Atmos. Chem. Phys., 17, 5703–5719, 2017
www.atmos-chem-phys.net/17/5703/2017/
doi:10.5194/acp-17-5703-2017

Atmospheric Chemistry and Physics
Open Access
EGU

Fine particle pH and gas–particle phase partitioning of inorganic species in Pasadena, California, during the 2010 CalNex campaign

Hongyu Guo[1], Jiumeng Liu[1,a], Karl D. Froyd[2,3], James M. Roberts[2], Patrick R. Veres[2,3], Patrick L. Hayes[3,4,5], Jose L. Jimenez[3,5], Athanasios Nenes[1,6,7,8], and Rodney J. Weber[1]

[1]School of Earth and Atmospheric Sciences, Georgia Institute of Technology, Atlanta, GA, USA
[2]Chemical Sciences Division, Earth System Research Laboratory, NOAA, Boulder, CO, USA
[3]Cooperative Institute for Research in Environmental Sciences (CIRES), Boulder, CO, USA
[4]Department of Chemistry, Université de Montéal, Montréal, Québec H3T 1J4, Canada
[5]Department of Chemistry and Biochemistry, University of Colorado Boulder, Boulder, CO, USA
[6]School of Chemical and Biomolecular Engineering, Georgia Institute of Technology, Atlanta, GA, USA
[7]Foundation for Research and Technology, Hellas, Greece
[8]National Observatory of Athens, Athens, Greece
[a]now at: Atmospheric Sciences and Global Change Division, Pacific Northwest National Laboratory, Richland, WA, USA

Correspondence to: Rodney J. Weber (rweber@eas.gatech.edu) and Athanasios Nenes (athanasios.nenes@gatech.edu)

Received: 23 December 2016 – Discussion started: 5 January 2017
Revised: 22 March 2017 – Accepted: 12 April 2017 – Published: 8 May 2017

Abstract. pH is a fundamental aerosol property that affects ambient particle concentration and composition, linking pH to all aerosol environmental impacts. Here, PM_1 and $PM_{2.5}$ pH are calculated based on data from measurements during the California Research at the Nexus of Air Quality and Climate Change (CalNex) study from 15 May to 15 June 2010 in Pasadena, CA. Particle pH and water were predicted with the ISORROPIA-II thermodynamic model and validated by comparing predicted to measured gas–particle partitioning of inorganic nitrate, ammonium, and chloride. The study mean ± standard deviation PM_1 pH was 1.9 ± 0.5 for the SO_4^{2-}–NO_3^-–NH_4^+–HNO_3–NH_3 system. For $PM_{2.5}$, internal mixing of sea salt components (SO_4^{2-}–NO_3^-–NH_4^+–Na^+–Cl^-–K^+–HNO_3–NH_3–HCl system) raised the bulk pH to 2.7 ± 0.3 and improved predicted nitric acid partitioning with $PM_{2.5}$ components. The results show little effect of sea salt on PM_1 pH, but significant effects on $PM_{2.5}$ pH. A mean PM_1 pH of 1.9 at Pasadena was approximately one unit higher than what we have reported in the southeastern US, despite similar temperature, relative humidity, and sulfate ranges, and is due to higher total nitrate concentrations (nitric acid plus nitrate) relative to sulfate, a situation where particle water is affected by semi-volatile nitrate concentrations. Under these conditions nitric acid partitioning can further promote nitrate formation by increasing aerosol water, which raises pH by dilution, further increasing nitric acid partitioning and resulting in a significant increase in fine particle nitrate and pH. This study provides insights into the complex interactions between particle pH and nitrate in a summertime coastal environment and a contrast to recently reported pH in the eastern US in summer and winter and the eastern Mediterranean. All studies have consistently found highly acidic PM_1 with pH generally below 3.

1 Introduction

Ambient aerosol particles affect human health and climate (Lim et al., 2012; IPCC, 2013), and have many other environmental effects. Particle pH is linked to all of these by altering the fundamental aerosol properties of particle mass and chemical composition. For example, some important pathways leading to secondary organic aerosol (SOA) formation from biogenic volatile organic compounds (VOCs), such as isoprene and α-pinene, are catalyzed by H^+ (Jang et al., 2002; Gao et al., 2004; Edney et al., 2005; Surratt et al.,

2007, 2010; Eddingsaas et al., 2010; Han et al., 2016). pH directly affects particle mass and composition through altering the partitioning of both semi-volatile inorganic and organic acids between particle and gas phases (Guo et al., 2016). pH affects the nitrogen cycle through gas–particle partitioning of HNO_3–NO_3^- and NH_3–NH_4^+, impacting deposition patterns due to large differences in gas versus particle dry deposition rates (Huebert and Robert, 1985; Duyzer, 1994; Schrader and Brummer, 2014).

Particle pH is linked to adverse health impacts, both directly and indirectly. Synergistic adverse health effects have been observed between ozone and acidic aerosols (Last, 1991; Enami et al., 2008) and epidemiological studies have reported adverse health outcomes associated with strong aerosol acidity (Koutrakis et al., 1988; Thurston et al., 1994; Dockery et al., 1996; Raizenne et al., 1996; Gwynn et al., 2000; Lelieveld et al., 2015). Low pH increases the solubility of transition metals, such as iron and copper (Meskhidze et al., 2003; Oakes et al., 2012; Longo et al., 2016; Fang et al., 2017), which have been linked to aerosol toxicity through aerosol oxidative effects (Ghio et al., 2012; Verma et al., 2014; Fang et al., 2015, 2017). Metal mobility also affects nutrient distributions with important impacts on photosynthesis productivity (Duce and Tindale, 1991; Meskhidze et al., 2003; Nenes et al., 2011; Ito and Xu, 2014; Myriokefalitakis et al., 2015; Li et al., 2017), carbon sequestration and ocean oxygen levels (Ito et al., 2016).

Due to limitations with direct particle pH measurement techniques, fine particle pH has often been indirectly inferred from aerosol composition based on ion balances or cation-anion molar balances, e.g., ammonium to sulfate (NH_4^+ / SO_4^{2-}) molar ratios. However, these are largely inaccurate pH proxies (Guo et al., 2015, 2016; Hennigan et al., 2015; Weber et al., 2016), which if used can provide misleading indications on the level of acidity present in the aerosol and pH-related properties. Alternatively, particle pH is more accurately calculated with a thermodynamic model, such as ISORROPIA-II (Nenes et al., 1998; Fountoukis and Nenes, 2007) or E-AIM (Clegg et al., 1998, 2003; Wexler and Clegg, 2002), which consider particle water, solution non-ideality, and variable dissociation of inorganic species in solution and equilibrium of semi-volatiles between gas and aerosol (aqueous and solid) phases. In "forward mode", which utilizes both gas- and particle-phase inputs, the accuracy of pH predictions can be assessed by comparing predicted to measured partitioning of semi-volatile species, such as NH_3–NH_4^+, HNO_3–NO_3^-, and HCl–Cl^- pairs. The semi-volatile species with the most information content about pH depend on the conditions at a specific location (e.g., when the specific component is not completely in the gas or particle phase).

This work adds to our investigation of particle pH in differing locations and under different emission characteristics. We have reported that ground-level pH in the southeastern US is 0.9 ± 0.6 (mean $\pm$ standard deviation, SD) in summer and 2.0 ± 1.0 in winter (Guo et al., 2015), and 0.8 ± 1.0 in the boundary layer and lower free troposphere (< 5 km altitude) over broad regions of the eastern US in winter, based on aircraft data (Guo et al., 2016.) A pH of 1.3 ± 1.1 has also been reported in various air masses advected to Crete in the eastern Mediterranean (Bougiatioti et al., 2016). This study focuses on particle pH in an urban coastal site, Pasadena, CA, and investigates the reasons for significantly higher nitrate mass loadings compared to those of the southeastern US (Zhang et al., 2007; Hand et al., 2012).

2 Methods

2.1 Sampling site

Aerosol and gas measurements were conducted on the California Institute of Technology campus in Pasadena, California (34.140582° N, 118.122455° W; altitude above sea level: 235 m), as part of the 2010 California Research at the Nexus of Air Quality and Climate Change (CalNex) campaign from 15 May to 15 June 2010 (Ryerson et al., 2013). The CalNex ground site was located within the Los Angeles Basin and approximately 16 km northeast of central Los Angeles (hereafter referred to as LA) and 5 km south of the San Gabriel Mountains. With the dominant wind from the southwest, the site was regularly impacted by emissions transported from the coast and central LA area (Washenfelder et al., 2011; Hayes et al., 2013). Meteorological data used in the following analysis are from the National Oceanic and Atmospheric Administration's (NOAA) CalNex researchers meteorological station.

2.2 Instrumentation

2.2.1 Particles

– PILS-IC: $PM_{2.5}$ (particles with aerodynamic diameters < 2.5 µm at ambient conditions) water-soluble ions were measured with a particle-into-liquid sampler coupled with ion chromatographs (PILS-IC), similar to that described elsewhere (Orsini et al., 2003; Hennigan et al., 2006; Sullivan et al., 2006; Peltier et al., 2007). The operation of PILS-IC during CalNex has been discussed by Liu et al. (2012) in detail. Ambient air was sampled through a URG (Chapel Hill, NC, USA) $PM_{2.5}$ cyclone and mixed with near 100 °C water vapor generated from deionized water. After growth, droplets were collected by impaction, producing a continuous liquid sample for online ion chromatograph analysis. All ambient data were blank-corrected by periodically measuring filtered ambient air. $PM_{2.5}$ anion data were available throughout the CalNex study, whereas cation data were only available for the last week (8–14 June). Since particle acidity predictions require both anion and cation data, discussions on $PM_{2.5}$ pH will include only the last

week of data. The measurement uncertainties of anions and cations, based on calibration variability, sample air flow rates, liquid flow rates, and field blanks, were estimated to be 13 % for anions and 8 % for cations. Detection limits were 0.015 $\mu g\,m^{-3}$ SO_4^{2-}, 0.03 $\mu g\,m^{-3}$ NO_3^-, 0.01 $\mu g\,m^{-3}$ Cl^- for anions, and 0.02 $\mu g\,m^{-3}$ NH_4^+, 0.02 $\mu g\,m^{-3}$ Na^+, 0.04 $\mu g\,m^{-3}$ K^+ for cations (Ca^{2+} and Mg^{2+} were not measured).

- AMS: PM_1 non-refractory inorganic and organic components were measured by a high-resolution time-of-flight aerosol mass spectrometer (HR-ToF-AMS, Aerodyne Research Inc., hereafter referred to as "AMS"; DeCarlo et al., 2006). The operation procedure of the AMS during this study has been described in Hayes et al. (2013) and measurement uncertainty estimated at 30 % (Middlebrook et al., 2012). The AMS detects non-refractory species in dried aerosols through an aerodynamic focusing lens, a detection chamber where aerosols are flash vaporized and ionized, followed by a time-of-flight mass spectrometer. The comparison of AMS PM_1 and PILS-IC $PM_{2.5}$ measurements was summarized in Hayes et al. (2013) and is discussed further below. In the following analysis PM_1 species are AMS data and $PM_{2.5}$ species are PILS-IC data.

- PALMS: single aerosol composition and size for diameters 0.15–3 µm were measured by an online particle analysis by laser mass spectrometer (PALMS) (Murphy et al., 2006; Froyd et al., 2010). In this method, individual aerosols scatter light from a continuous laser beam and trigger an excimer laser that ionizes the single particle. The resulting ions are analyzed by a time-of-flight mass spectrometer to generate a complete positive or negative mass spectrum per particle. In this study, PALMS data provide insights into the aerosol mixing state.

2.2.2 Gases

- QC-TILDAS: gas-phase NH_3 was quantified using a quantum cascade tunable infrared laser differential absorption spectrometer (QC-TILDAS), developed by Aerodyne Research Inc. and described in details in Ellis et al. (2010). QC-TILDAS uses a thermoelectrically cooled pulsed quantum cascade (QC) laser, which measures NH_3 at 967 cm^{-1} in the infrared regime. The laser beam is directed into an astigmatic Herriot absorption cell, where it passes between two highly reflective mirrors before leaving the cell and arriving at a thermoelectrically cooled mercury cadmium telluride (HgCdTe) infrared detector. A 12 m heated ($40 \pm 2\,^{\circ}C$) and insulated 0.95 cm perfluoroalkoxy (PFA) line (Clayborn Lab, Truckee, CA, USA) connects a short (10 cm; 8 m above ground) custom-designed quartz inlet to the QC-TILDAS. The inlet includes two ports for the introduction of calibration and background gas designed so that the flows follow the same path through the inlet as the ambient sample. Zero-air measurements and ammonia calibrations were performed periodically during the CalNex campaign. The detection limit was 1.5 ppbv for 1 s data and decreased to 0.42 ppbv for 1 min averaging data. The overall NH_3 measurement uncertainty was 10 %.

- NI-PT-CIMS: gas-phase HNO_3 and HCl measurements were made using a negative-ion proton-transfer chemical ionization mass spectrometer (NI-PT-CIMS; hereafter referred to as "CIMS"). Details of the NI-PT-CIMS design and operation during CalNex have been reported in Veres et al. (2008). Acidic molecules are ionized by proton transfer with acetate ions and detected as conjugate anions with a quadrupole mass spectrometer. The CIMS was placed on top of an instrument trailer at 3 m height with a heated (75 °C) 0.32 cm Teflon inlet, 1.3 m in length, sampling at 5 m relative to ground level. (Possible biases in measured HNO_3 and HCl due to aerosol volatilization in the heated inlet is discussed in Sect. 4.1). In the field, instrument backgrounds were quantified every 190 min for a duration of 30 min. The detection limits were 0.080 ppbv for HNO_3 and 0.055 ppbv for HCl. Overall measurement uncertainty was 35 %. All gas-phase concentrations reported in ppbv were converted to $\mu g\,m^{-3}$ at ambient conditions to be consistent with particle-phase measurements and for thermodynamic calculations. In all cases, gas and particle concentrations are reported and utilized in the model using ambient conditions (i.e., all volumetric concentrations are at ambient temperature and pressure).

2.3 pH and gas–particle partitioning modeling

pH is defined as the negative logarithm of the hydronium ion (H_3O^+) activity in an aqueous solution. Hereafter we denote H_3O^+ as H^+ for simplicity, while recognizing that the unhydrated hydrogen ion is rare in aqueous solutions. pH is given by

$$\mathrm{pH} = -\log_{10}\gamma_{H^+} H^+_{aq} = -\log_{10}\frac{1000\gamma_{H^+} H^+_{air}}{W_i + W_o} \cong -\log_{10}\frac{1000\gamma_{H^+} H^+_{air}}{W_i}, \quad (1)$$

where γ_{H^+} is the hydronium ion activity coefficient (in this case assumed = 1), H^+_{aq} (mole L^{-1}) the hydronium ion concentration in particle liquid water, H^+_{air} ($\mu g\,m^{-3}$) the hydronium ion concentration per volume of air, and W_i and W_o ($\mu g\,m^{-3}$) the bulk particle water concentrations associated with inorganic and organic species, respectively. W_o can be calculated by Eq. (5) in Guo et al. (2015). Both H^+_{air} and W_i are outputs of the thermodynamic model, ISORROPIA-II,

which was used to determine the composition and phase state of an NH_4^+–SO_4^{2-}–NO_3^-–water inorganic aerosol in thermodynamic equilibrium with its corresponding gases. (In some cases Cl^--Na^+-K^+ were also included). A similar approach has been used in several studies for contrasting summer and winter conditions in the eastern US (Guo et al., 2015, 2016; Weber et al., 2016) and eastern Mediterranean (Bougiatioti et al., 2016, 2017).

In previous studies, the effect of W_o on pH has been investigated and found to be minor (Guo et al., 2015). pH in that study based solely on W_i was 0.15–0.23 units systematically lower than pH predicted with total particle water ($W_i + W_o$) and highly correlated ($R^2 = 0.97$). In this study, ΔpH values of +0.12 and +0.19 units were estimated when including W_o based on average and maximum organic hygroscopic parameter κ_{org} of 0.13 and 0.23, respectively (Mei et al., 2013). Sensitivity of pH to effects of W_o are smaller in CalNex due to smaller fractions of W_o to total particle water (21 %) compared to that found in SOAS (Southern Oxidant and Aerosol Study; 35 %). Given this relatively small deviation (on average 0.12 unit), we report pH only considering W_i.

ISORROPIA-II was run assuming particles were "metastable" with no solid precipitates (H^+ is not stable in an effloresced aerosol) – a reasonable assumption considering the high RH range observed during this study (mean $\pm$ SD of RH $= 79 \pm 17$ %). In our previous pH studies, we only considered data for RH between 20 and 95 %. At low RH (e.g., < 20 %), aerosols are less likely to be in a completely liquid state (Ansari and Pandis, 2000; Malm and Day, 2001; Fountoukis and Nenes, 2007; Bertram et al., 2011), and the "glassy" SOA may impede the partitioning of semi-volatile species due to decreased diffusion in the particles (Ye et al., 2016), and uncertainties in predicted pH are expected to be large due to uncertain activity coefficients associated with highly concentrated solutions (Fountoukis et al., 2009). At RH > 95 %, large pH uncertainty is introduced due to the exponential growth in particle liquid water with RH and propagation of RH sensor uncertainties (Malm and Day, 2001; Guo et al., 2015). The CalNex RH ranged from 22 to 100 %; therefore periods for RH above 95 % were excluded.

The model was also run in "forward" mode, which calculates the gas–particle equilibrium partitioning concentrations based on the input of total concentration of a species (i.e., gas + particle). Use of total species as ISORROPIA-II inputs produces substantially better predictions compared with only particle-phase concentration inputs in either "forward" or "reverse" modes since in the former cases ("forward" mode with only particle-phase input), particle-phase semi-volatile species concentration is underpredicted due to some fraction repartitioned into the gas phase in the model, and in the latter cases ("reverse" mode), measurement errors often result in large model biases in pH (Hennigan et al., 2015).

The predicted gas- or particle-phase semi-volatile compounds can be compared to measurements for validating the thermodynamic calculations. Possible partitioning pairs for ISORROPIA-II are HNO_3–NO_3^-, NH_3–NH_4^+, and HCl–Cl^- (discussed in Sect. 3.2 and 3.3). This method is effective when gas- and particle-phase components have substantial fractions in both the gas and particle phases. For example, in the southeastern US in summer, ammonia partitioning (gas/(gas + particle)) varied between 10 and 80 %, whereas nitric acid partitioning was mostly near 80 % and PM_1 nitrate level close to the detection limit (larger uncertainty), making ammonia partitioning much more useful than nitric acid for evaluating thermodynamic models (Guo et al., 2015). In contrast, nitric acid partitioning ranged from 0 to 100 % (average $\sim$ 50 %) and so was used to evaluate pH predicted in the northeastern US in the cold season (Guo et al., 2016).

Using gas–particle phase partitioning to constrain particle pH can be complicated by the presence of multiple phases within the particle, which may distribute inorganic species amongst multiple phases, each with their own water activity and hence inorganic concentration. Lab studies show that liquid–liquid phase separations are always observed at O : C (organic aerosol atomic O to C ratio) ≤ 0.5, whereas no phase separations occur for O : C ≥ 0.8 (Bertram et al., 2011; Song et al., 2012; You et al., 2013, 2014). The likelihood for phase separation decreases at higher RH ($0.5 <$ O:C < 0.8) and only has a weak dependence on T (Schill and Tolbert, 2013; You and Bertram, 2015). For conditions during SOAS (O : C $= 0.75 \pm 0.12$, RH $= 74 \pm 16$ %, $T = 25 \pm 3$ °C), we found that thermodynamic calculations accurately predicted bulk particle water and ammonia partitioning over the complete T (18 to 33 °C) and RH (36 to 96 %) ranges (Guo et al., 2015). During the Wintertime Investigation of Transport, Emissions, and Reactivity (WINTER) aircraft study (O : C $= 0.78 \pm 0.11$, $T = 0 \pm 8$ °C), we found that HNO_3–NO_3^- partitioning was accurately predicted for RH > 60 % (Guo et al., 2016). Compared to SOAS and WINTER (both in the eastern US), in this study the smaller O : C (0.52 ± 0.10) (Hayes et al., 2015) means we cannot outright exclude the possibility of phase separation, but very high RH (79 ± 17 %) makes it less likely.

In running ISORROPIA-II to predict pH and semi-volatile species partitioning, it is also assumed that the particles are internally mixed, that pH does not vary with particle size (i.e., bulk properties represent the overall aerosol pH), and that the ambient aerosols and gases are in thermodynamic equilibrium. For the WINTER study, which included measurements over coastal and marine areas, we found that PM_1 pH was accurately predicted with only particle-phase SO_4^{2-}, NO_3^-, and NH_4^+ (and gas-phase HNO_3), whereas sea salt components had some, but generally small, effects on the prediction of particle pH (except on rare occasions when the mole fraction of NaCl to total soluble inorganic ions was greater than 50 %) (Guo et al., 2016). The mixing state of sea salts with SO_4^{2-}, NO_3^-, and NH_4^+ is a critical issue in predicting particle pH in LA and is discussed below.

3 Results

3.1 PM_1 and $PM_{2.5}$ inorganic composition and gas–particle partitioning

Time series for various measured parameters during CalNex are shown in Fig. 1. CalNex T and RH were $18 \pm 4\,^{\circ}C$ and $79 \pm 17\,\%$ (mean $\pm$ SD). During the first half of the campaign, 15 to 29 May, daily maximum T was below 26 °C and PM_1 (AMS) and $PM_{2.5}$ (PILS-IC) SO_4^{2-}, NO_3^-, and NH_4^+ showed a general decreasing trend ($PM_{2.5}$ NH_4^+ data were not available in this period). The second half of the campaign started with a warmer period (30 May to 7 June), with the highest T reaching 29 °C. During this period, SO_4^{2-}, NO_3^-, NH_4^+, and HNO_3 were significantly higher than the first half and reached campaign maximums of $9.7\,\mu g\,m^{-3}$ PM_1 SO_4^{2-}, $20.1\,\mu g\,m^{-3}$ PM_1 NO_3^-, $9.6\,\mu g\,m^{-3}$ PM_1 NH_4^+, and $33.1\,\mu g\,m^{-3}$ HNO_3. The peak concentrations of combined PM_1 inorganics alone exceeded the National Ambient Air Quality Standards (NAAQS) $PM_{2.5}$ 24 h limit of $35\,\mu g\,m^{-3}$ (https://www.epa.gov/criteria-air-pollutants/naaqs-table), with the largest contribution from NO_3^-. Gaseous components other than HNO_3, such as NH_3 and HCl, showed different patterns than the above species, indicating different sources and sinks.

PM_1 (AMS) SO_4^{2-}, NO_3^-, and NH_4^+ were highly correlated with $PM_{2.5}$ (PILS-IC) measurements, with R^2 between 0.8 and 0.9 (Fig. S1). PM_1 / $PM_{2.5}$ mass ratios were $97.5 \pm 5.4\,\%$ for SO_4^{2-}, $63.5 \pm 22.1\,\%$ for NO_3^-, and $92.3 \pm 9.9\,\%$ for NH_4^+. Note that the mass fractions for SO_4^{2-} and NO_3^- are campaign averages, but NH_4^+ mass fraction is only for the last week when $PM_{2.5}$ NH_4^+ was available. Nearly 40 % of the NO_3^- was found between 1 and 2.5 µm, whereas most SO_4^{2-} and NH_4^+ were associated with PM_1. (Ratios based on regression slopes are shown in Fig. S1.) Hence, the NO_3^- for the 1 to 2.5 µm size range was likely associated with some non-volatile cations, such as Na^+ and K^+ instead of NH_4^+. The $PM_{2.5}$ Cl^- / Na^+ molar ratio was 0.5 ± 0.2. Given that these species are mainly transported from the coastal regions in the form of sea salts (NaCl), this indicates that roughly half of the Na^+ had reacted with HNO_3 resulting in depleted Cl^- (Robbins et al., 1959; Langer et al., 1997). These results are consistent with the analysis of Hayes et al. (2013).

Measurements of semi-volatile particle (NO_3^-, NH_4^+, Cl^-) and corresponding inorganic gases (HNO_3, NH_3, HCl) are used to investigate partitioning. The gas–particle phase partitioning is described as the particle-phase mass concentration divided by the total mass concentration (gas + particle), e.g., $\varepsilon(NO_3^-) = NO_3^- / (HNO_3 + NO_3^-)$. The campaign average partitioning ratios were as follows: for PM_1 $\varepsilon(NO_3^-) = 39 \pm 16\,\%$, PM_1 $\varepsilon(NH_4^+) = 56 \pm 26\,\%$, $PM_{2.5}$ $\varepsilon(NO_3^-) = 54 \pm 10\,\%$, and $PM_{2.5}$ $\varepsilon(Cl^-) = 39 \pm 26\,\%$. All partitioning ratios are near 50 %, making them useful for assessing pH predictions by comparing measured versus ISORROPIA-predicted ratios.

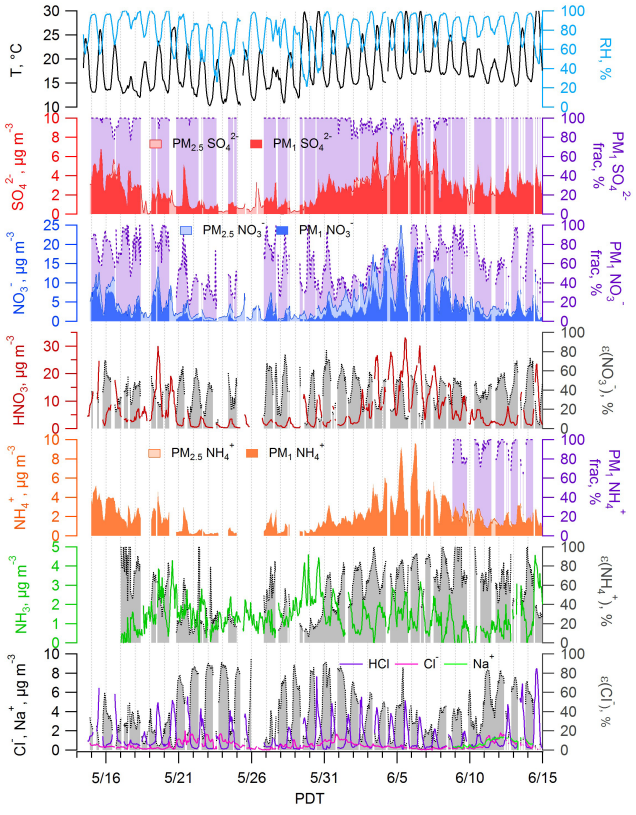

Figure 1. CalNex campaign time series of meteorological conditions (T, RH), particle- and gas-phase inorganic compound mass loadings (SO_4^{2-}, NO_3^-, Cl^-, NH_4^+, Na^+; HNO_3, NH_3, HCl), particle-phase mass fractions of total (gas plus particle; $\varepsilon(NO_3^-)$, $\varepsilon(NH_4^+)$ based on PM_1 and $\varepsilon(Cl^-)$ based on $PM_{2.5}$, all denoted by grey shading), and PM_1 to $PM_{2.5}$ mass fractions of SO_4^{2-}, NO_3^-, and NH_4^+ (all denoted by purple shading).

3.2 PM_1 pH prediction and verification

PM_1 pH was determined to be on average ($\pm$SD) 1.9 ± 0.5 for the complete study, for model inputs of PM_1 inorganic AMS-measured components SO_4^{2-}, NO_3^-, and NH_4^+ and gases HNO_3 and NH_3. Although the CalNex ground site was influenced by sea salt components, Na^+ and Cl^- were not included in the PM_1 pH since NaCl is typically found mainly at sizes above 1 µm and the mixing states of PM_1 NaCl with SO_4^{2-}, NO_3^-, and NH_4^+ remains to be investigated. PALMS single-particle data indicated that for the particle size range with D_{ve} (dry volume-equivalent diameter) between 0.15 and 780 nm ($\sim$ 1 µm), by number 27 % of PM_1 sea salt particles (Na^+-rich particles without crustal materials) had observable NO_3^- signals and by mass only 12 % of PM_1 are sea salt types

Table 1. Number fraction of sea salt particles with observable nitrate signals and mass fraction of sea salt particles to total mass in two size ranges, 0.15–1 and 1–2.5 µm. Sea salt particles are identified as Na^+-rich particles without crustal elements. The number fraction was determined directly from the PALMS data and the mass fraction was calculated based on the number fractions and size distributions, assuming dry particle densities.

Particle size, µm	Number fraction of sea salt particles with observable nitrate signal	Sea salt particles mass fraction to total
0.15–1	27 %	12 %
1–2.5	85 %	63 %

(Table 1), suggesting external mixing of NaCl with NO_3^- is the main form. For the 1 to 2.5 µm size range the number and mass fractions were 85 and 63 %, respectively.

We assess predicted pH from the thermodynamic model by comparing predicted and measured gas–particle partitioning of NH_3–NH_4^+ and HNO_3–NO_3^-. Comparison of HNO_3–NO_3^- and NH_3-NH_4^+ predictions to their measured values is shown as Fig. 2. Gas-phase HNO_3 and NH_3 and particle-phase NH_4^+ are on average within 10 % and highly correlated, $R^2 > 0.8$. Despite a high correlation ($R^2 = 0.76$), ISORROPIA-II predicted particle-phase NO_3^- is systematically higher than observed, with a regression slope of 1.28. Two bands are observed that are related to RH or time of day (Fig. 2b); for mid-range RH (50–70 %) daytime data, ISORROPIA-II slightly underpredicts NO_3^- and for high RH (∼ 90 %) nighttime data, NO_3^- is overpredicted. This leads to a regression slope of 2 comparing predicted to measured $\varepsilon(NO_3^-)$ and a large intercept (Fig. 2c, also see Fig. S5). In contrast, predicted versus measured $\varepsilon(NH_4^+)$ is close to 1 : 1 and highly correlated ($R^2 = 0.8$, Fig. 2f), and there is a much weaker systematic variability related to RH or time of day.

3.3 $PM_{2.5}$ pH prediction and verification

Predicting the bulk pH of $PM_{2.5}$ is more complicated since the particles larger than 1 µm in the $PM_{2.5}$ fraction are not necessarily in equilibrium due to increased timescale for equilibration (> 20–30 min) (Fountoukis et al., 2009), especially in an environment with rapidly changing concentrations of key species (e.g., HNO_3). This leads to greater uncertainty when predicting partitioning of semi-volatile species. Furthermore, the pH analysis now needs to consider sea salt components (SO_4^{2-}–NO_3^-–NH_4^+–Na^+–Cl^-–K^+–HNO_3–NH_3–HCl system). Whereas single-particle PALMS data suggested that only a small fraction (27 %) of the sea salt particles less than 1 µm were internally mixed with nitrate, for sizes between 1 and 2.5 µm, the majority (85 %) were. Overall we find bulk $PM_{2.5}$ pH considering sea salt components higher than PM_1 by 0.8 units on average. For data from the last week of the study (i.e., period of PILS data that in-

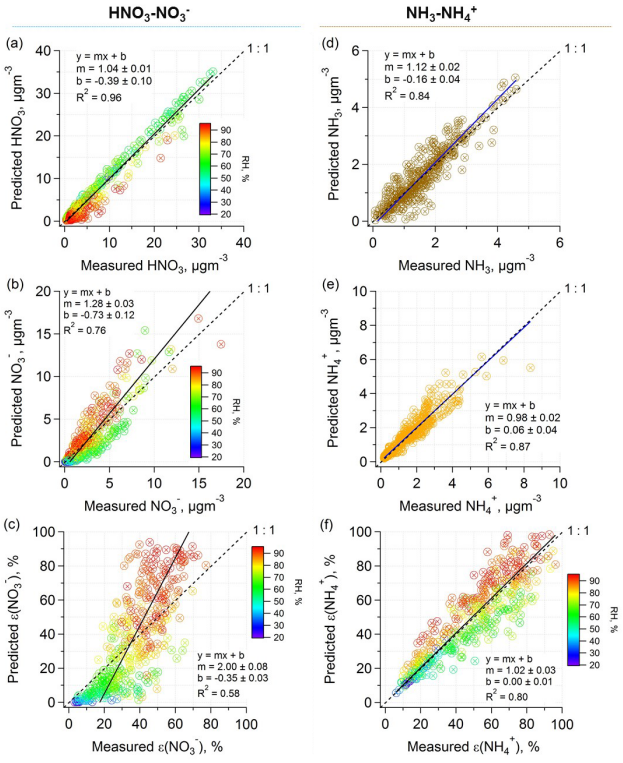

Figure 2. Comparisons of predicted and measured HNO_3, NO_3^-, and $\varepsilon(NO_3^-)$ **(a, b, c)** and NH_3, NH_4^+, and $\varepsilon(NH_4^+)$ **(d, e, f)** for data from the complete CalNex study. Particle-phase data are all AMS PM_1. Orthogonal distance regression (ODR) fits are shown and uncertainties in the fits are 1 standard deviation.

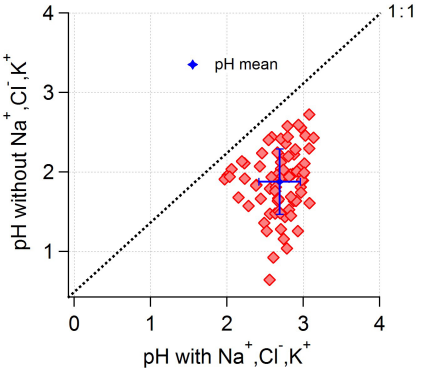

Figure 3. Comparison of predicted $PM_{2.5}$ particle pH assuming external versus internal mixing of Na^+, Cl^-, and K^+ with SO_4^{2-}, NO_3^-, and NH_4^+ for data from the last week of the CalNex study (i.e., SO_4^{2-}–NO_3^-–NH_4^+–HNO_3–NH_3 system vs. SO_4^{2-}–NO_3^-–NH_4^+–Na^+–Cl^-–K^+–HNO_3–NH_3–HCl system). For these two cases, pH increased from 1.9 ± 0.4 to 2.7 ± 0.3 with the input of Na^+, Cl^-, and K^+. Figures 4 and 5 show that for $PM_{2.5}$, inclusion of Na^+, Cl^-, and K^+ provides better predicted portioning of nitric acid.

cludes measurements of sea salt components), PM_1 pH was 1.9 ± 0.4, similar to that of the complete study (1.9 ± 0.5), and in contrast to an average $PM_{2.5}$ pH of 2.7 ± 0.3. A comparison of the pH is shown in Fig. 3. Addition of non-volatile Na^+ and K^+ increases pH. Na^+ is the more important cation in this case, as the Na^+ levels were several times larger than K^+ (0.77 ± 0.39 vs. $0.20 \pm 0.09\,\mu g\,m^{-3}$, or 0.33 vs. $0.05\,mol\,m^{-3}$).

To examine the effects of sea salt components on the thermodynamic predictions, we compared the observed to measured partitioning of $PM_{2.5}$ semi-volatile species in Fig. 4. ISORROPIA-II was run with two differing inputs, one with Na^+, Cl^-, and K^+ and the other run without these ions. In both cases only PILS-IC $PM_{2.5}$ data are used. All other input parameters, including NH_4^+, SO_4^{2-}, NO_3^-, RH, and T, were the same. Figure 4 shows that inclusion of Na^+, Cl^-, and K^+ improves the prediction of HNO_3–NO_3^- partitioning. For HNO_3, NO_3^-, and $\varepsilon(NO_3^-)$, predicted levels are somewhat closer to the measurements and the scatter in the data is reduced. However, like the PM_1 analysis above, the slope between predicted and measured $\varepsilon(NO_3^-)$, 2.4, is significantly larger than 1. The deviation is again related to RH, resulting from a diurnal dependence. Unlike the HNO_3–NO_3^- partitioning, NH_3-NH_4^+ partitioning is not as sensitive to inclusion of Na^+, Cl^-, and K^+. Overall, $\varepsilon(NH_4^+)$ is on average underestimated by 17 % compared to measured (average ratio). HCl–Cl^- partitioning is well captured by ISORROPIA-II with regression slopes of 1.05, 0.95, and 1.14 and R^2 of 0.98, 0.84, and 0.81 for HCl, Cl^-, and $\varepsilon(Cl^-)$, respectively.

An analytical calculation of HNO_3–NO_3^- partitioning can also be used to assess whether the shift of one pH unit caused by Na^+, Cl^-, and K^+ is consistent with observed nitric acid partitioning for $PM_{2.5}$. The analytical calculation is based on Eq. (3) in Guo et al. (2016) and a detailed equation derivation can be found in Supplement Sect. S2. To minimize the effects of T and W_i variability on partitioning, and focus on the role of pH, data for a relatively small T (17–23 °C) and W_i (5–15 $\mu g\,m^{-3}$) range were selected. Predicted activity coefficients, γ_{H^+} and $\gamma_{NO_3^-}$, extracted from ISORROPIA-II, were input in the analytical calculation to account for solution non-ideality. The product of the activity coefficients, $\gamma_{H^+}\gamma_{NO_3^-}$, was on average 0.28 with Na^+, Cl^-, and K^+ in the model and 0.19 without Na^+, Cl^-, and K^+ ($\gamma_{H^+}\gamma_{NO_3^-}$ is smaller without Na^+, Cl^-, and K^+ due to less predicted W_i, thus overall larger ionic strength). The analytical calculated S curves are plotted with the measurements and ISORROPIA-II predictions in Fig. 5. As noted, including these components changes the activity coefficient $\gamma_{H^+}\gamma_{NO_3^-}$ (as can be seen by the difference in the two curves in Fig. 5) and also slightly increases the liquid water. But the most important effect is reducing H^+, resulting in a shift to higher pH. This analysis also shows that the measured $\varepsilon(NO_3^-)$ comes into better agreement with its theoretical S curve for the SO_4^{2-}–NO_3^-–NH_4^+–Na^+–Cl^-–K^+–HNO_3–NH_3–HCl system (red points closer to red curve compared to blue points and blue curve). Similar to $\varepsilon(NO_3^-)$, measured $\varepsilon(Cl^-)$ is also found to be in good agreement with the S curve (Fig. S2).

3.4 Average diurnal trends

– PM_1: the diurnal variations in T, RH, pH, LWC, and HNO_3–NO_3^-, and NH_3–NH_4^+ partitioning are shown together in Fig. 6. Due to the inverse variation between T and RH diurnal patterns, predicted particle water (W_i) reached a daily maximum before dawn and decreased rapidly with RH after sunrise. To be consistent with pH, particle water data are not plotted for RH above 95 %. (For RH above 95 %, particle water increased continuously at night until reaching the daily highest RH at 05:30.) Between 13:00 and 20:00 LT (local time), W_i stayed consistently low ($\sim 5\,\mu g\,m^{-3}$). PM_1 pH generally tracked liquid water. pH was lower in the daytime due to less liquid water, reaching a minimum value of 1.6 at approximately 16:00. After that, pH continued to increase to its daily maximum of 2.4 at midnight, tracking the liquid water concentrations. This pH diurnal pattern is similar to that observed in the southeastern US (Guo et al., 2015). A very large peak in gaseous HNO_3 was observed during the day produced from rapid photochemical reactions of NO_x with the hydroxyl radical in the LA outflows (Veres et al., 2011). In contrast, NO_3^- peaked at dawn under conditions of low T and high RH, which favored nitrate condensation (S curves shifted to lower pH; see Fig. S3 and S4), consistent with a previous study in Mexico City (Hennigan et al., 2008). There was also a small peak in NO_3^- near midday when HNO_3 peaked, simply due to the large amount of fresh HNO_3, despite the trend of a continuous $\varepsilon(NO_3^-)$ decrease. The diurnal variation in $\varepsilon(NO_3^-)$ was similar to liquid water and pH. The PM_1 NH_4^+ trend followed NO_3^- and all inorganic species (NH_4^+, SO_4^{2-}, NO_3^-) exhibited a peak during the day. $\varepsilon(NH_4^+)$ had a similar diurnal pattern to $\varepsilon(NO_3^-)$.

– $PM_{2.5}$: Fig. 7 compares the diurnal trends of PM_1 pH (AMS data, SO_4^{2-}, NO_3^-, NH_4^+) and $PM_{2.5}$ pH (PILS-IC SO_4^{2-}, NO_3^-, NH_4^+, Na^+, Cl^-, K^+) for the last week of the study. PM_1 pH had a similar profile to that for the complete study – lower in the afternoon and following the W_i trend – whereas the $PM_{2.5}$ diurnal pH trend was nearly flat. The difference was caused by more non-volatile Na^+ than volatile Cl^- ($PM_{2.5}$ Cl^- / Na^+ molar ratio was 0.5 ± 0.2), which is related to the HNO_3 and HCl trends. Sea salt components in the 1 to 2.5 µm size range react with the daytime high HNO_3 forming NO_3^- and gas-phase HCl (simplified as $Cl^- + HNO_3 \rightarrow NO_3^- + HCl$) (Robbins et al., 1959;

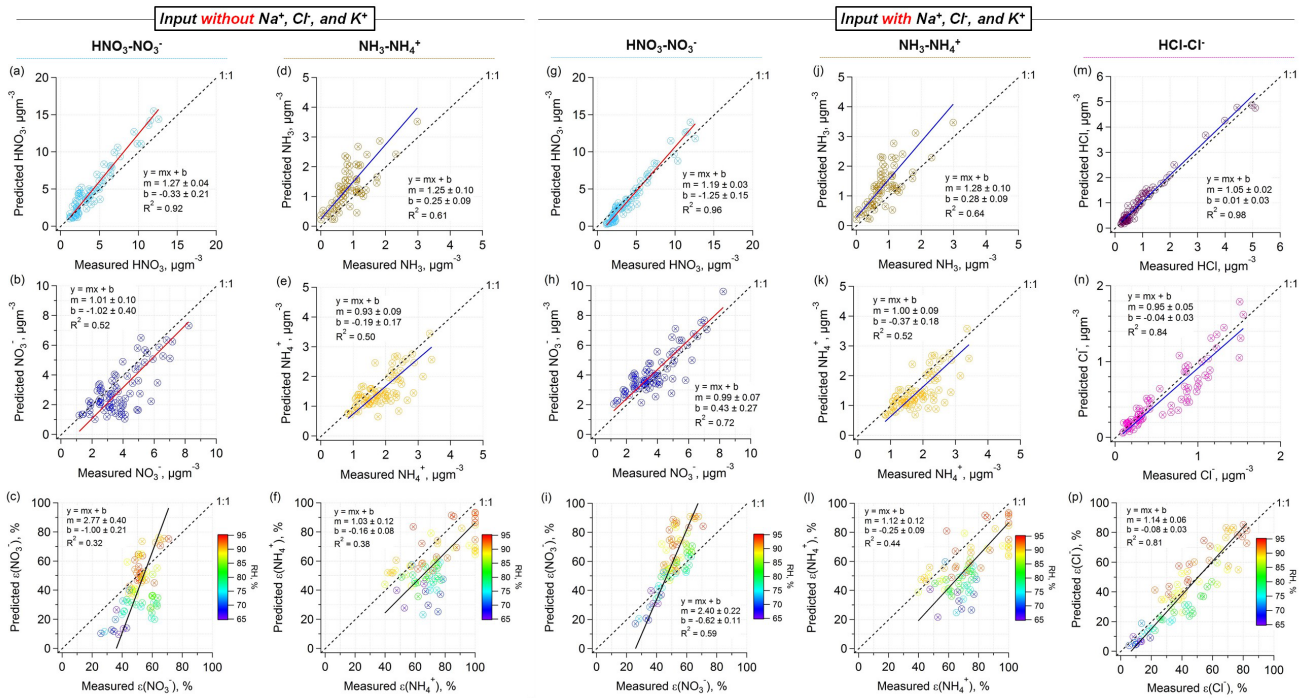

Figure 4. Intercomparisons of predicted and measured gas–particle phase partitioning for $PM_{2.5}$ particles for two scenarios: ISORROPIA-II input without (left) and with (right) Na^+, Cl^- (and HCl), and K^+. The other input SO_4^{2-}, NO_3^-, NH_4^+, NH_3, HNO_3, RH, and T are the same in the two cases. The $PM_{2.5}$ data for the last week during CalNex study are shown above. ODR fits are applied.

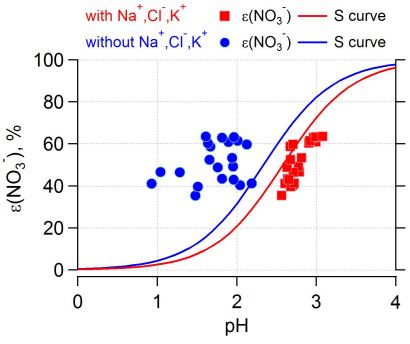

Figure 5. Comparison of measured $\varepsilon(NO_3^-)$ for $PM_{2.5}$ (data points) to S curves, which are predicted from theory and include activity coefficients from ISORROPIA-II. The product of the activity coefficients, $\gamma_{H^+}\gamma_{NO_3^-}$, was on average 0.28 with Na^+, Cl^-, and K^+ and 0.19 without Na^+, Cl^-, and K^+. In both cases pH (data points) is predicted by ISORROPIA-II.

Langer et al., 1997). This "chloride depletion" is a result of the higher volatility of HCl versus HNO_3 in the deliquesced sea salt aerosol (Nenes et al., 1998; Fountoukis and Nenes, 2007). The process can partly account for the large HCl peak and stronger Cl^- depletion (wider gap between Na^+ and Cl^-) during the day, coinciding with high HNO_3 and low W_i (evaporation of HCl occurs during evaporation of droplets). The slightly higher Na^+ generally increased pH due to the added non-volatile cations. These data are consistent with the discussion above indicating that bulk $PM_{2.5}$ pH is higher due to the contributions of sea salt aerosol components solely in the 1 to 2.5 μm range. For smaller particles (PM_1), these components do not significantly affect the SO_4^{2-}–NO_3^-–NH_4^+–HNO_3–NH_3 system resulting in a lower bulk PM_1 pH. Size-resolved particle pH and solubility of metals, reported in another study, are consistent with these findings (Fang et al., 2017). (Note that an attempt to calculate pH in the PM_1 to $PM_{2.5}$ size range was not successful due to highly uncertain data resulting from particle concentrations determined by difference from two separate measurements.)

4 Discussion

4.1 Cause for bias in $\varepsilon(NO_3^-)$

The bias between ISORROPIA-predicted and observed nitrate partitioning may be a result of several causes. Since the $\varepsilon(NO_3^-)$ bias is seen for both PM_1 (AMS data) and $PM_{2.5}$ (PILS-IC data), the cause is apparently not associated with a specific aerosol measurement method. For the aerosol measurements, sampling artifacts associated with differences in

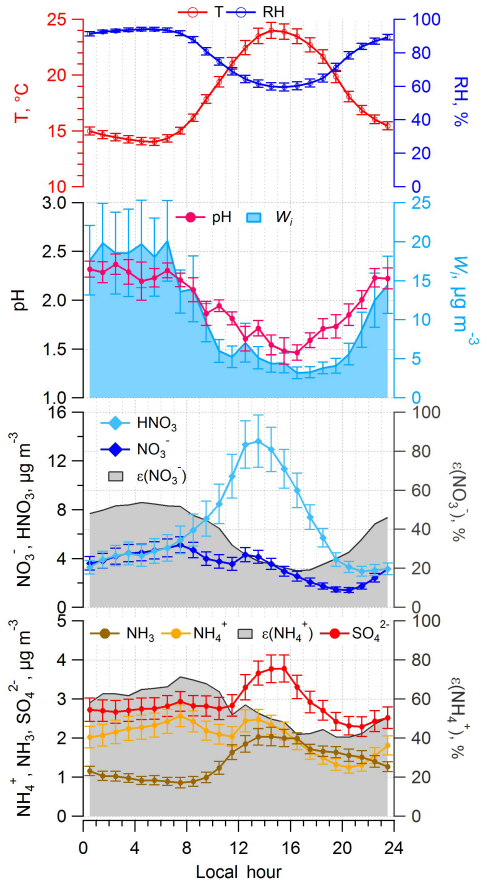

Figure 6. Diurnal profiles of predicted pH, LWC, and measured T, RH, particle- and gas-phase inorganic compound mass loadings (SO_4^{2-}, NO_3^-, NH_4^+, HNO_3, NH_3), and particle-phase fractions ($\varepsilon(NO_3^-)$ and $\varepsilon(NH_4^+)$). Data shown above are for the complete CalNex campaign, and particle-phase data are AMS PM_1. Mean hourly averages are shown and standard errors are plotted as error bars.

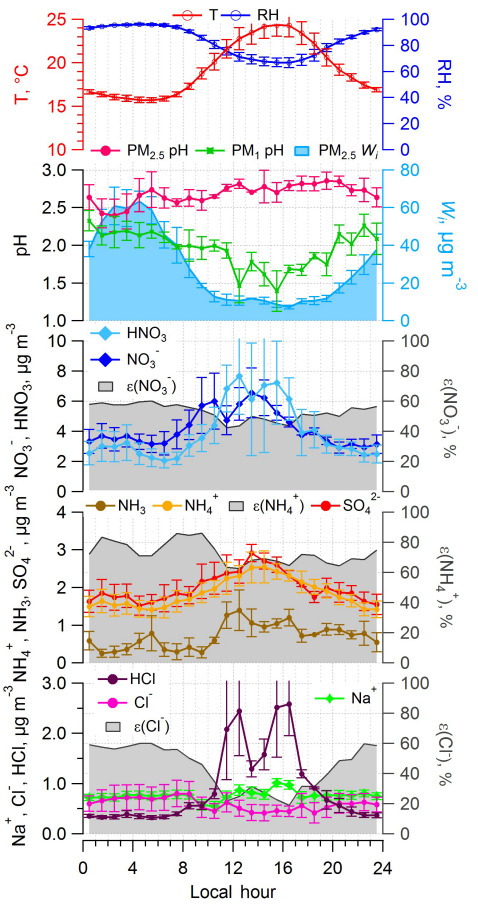

Figure 7. Diurnal profiles for the last week of CalNex of predicted pH and LWC, and measured T, RH, particle- and gas-phase inorganic compound mass loadings (SO_4^{2-}, NO_3^-, Cl^-, NH_4^+; HNO_3, NH_3, HCl), particle-phase fractions ($\varepsilon(NO_3^-)$, $\varepsilon(NH_4^+)$, $\varepsilon(Cl^-)$). Particle-phase data are all PILS-IC $PM_{2.5}$. Median hourly averages are shown, and standard errors are plotted as error bars.

indoor–outdoor temperatures that varied with time of day could be one cause for the biases. Sample heating is most likely to occur at night (indoor T > ambient T) and can cause semi-volatile NO_3^- loss, whereas sample cooling during the day (indoor T < ambient T) can lead to vapor condensation and higher NO_3^-. Differences in observed versus predicted NO_3^- are consistent with these trends (Fig. S5); measured NO_3^- is lower than predicted at night (negative artifact) and higher than predicted during the day (positive artifact). The same will apply to NH_3-NH_4^+ partitioning, but to a lesser degree due to the addition of non-volatile sulfate. Indoor temperatures were recorded to be fairly constant at ∼ 25 °C for the AMS trailer (Fig. S6, PILS trailer indoor temperatures are expected to be similar). Aerosol samples were heated by ∼ 10 °C at night and negligibly during the middle of the day (Table S1). Possible biases due to effects of the altered RH and T on aerosol measurements were examined by comparing measurements to model results for partitioning of HNO_3–NO_3^- and NH_3–NH_4^+ using sample line versus ambient conditions (Figs. S6 and S7), with all other model inputs the same. We find that ambient RH and T result in better agreement for NO_3^-, $\varepsilon(NO_3^-)$, NH_4^+, and $\varepsilon(NH_4^+)$, although some minor effect may be possible. We note that more extreme ambient to sample line temperature differences were experienced during the WINTER aircraft campaign (ΔT on average +24 °C). In that case, a similar analysis also found no evidence for nitrate loss due to sample line heating (Guo et al., 2016). (Sample-line residence times of 0.5 to 2 s are in the same range for both studies.)

The sampling systems for HNO_3 and NH_3 involved heated sample inlets, which could also lead to bias due to evaporation of aerosol components. Here we only focus on the CIMS sampling line heating (75 °C) since it was more extreme than the NH_3 (40 °C). For the CIMS system, a 75 °C inlet may cause particle nitrate and chloride evaporation (residence time = 0.32 s, Table S1), resulting in over-measurement of

HNO_3 and HCl (the species measured by this instrument). To examine whether this is the cause for the differences in predicted and observed $\varepsilon(NO_3^-)$, we compared the partitioning of HNO_3–NO_3^- and NH_3–NH_4^+ based on "corrected" HNO_3 assuming 10, 20 and 30 % of the measured NO_3^- evaporated in the CIMS inlet (the "corrected" HNO_3 is lower by subtracting the various fractions of PM_1 NO_3^- from measured HNO_3). Comparing the orthogonal regression fitting lines in the Fig. S8, only slight improvements in predicted to measured $\varepsilon(NO_3^-)$ are found for increased NO_3^- loss (Fig. S8c), but all lines converge at the same intercept. At 30 % evaporation the comparison becomes worse for both $\varepsilon(NO_3^-)$ and $\varepsilon(NH_4^+)$. We conclude that potential inlet artifacts associated with the aerosol- or gas-phase sampling systems cannot explain the predicted versus measured $\varepsilon(NO_3^-)$ bias. This is consistent with the limited inlet heating and residence times in this study compared to some thermodenuder studies utilizing more extreme conditions (Huffman et al., 2009; Riipinen et al., 2010).

Another possible cause of the $\varepsilon(NO_3^-)$ bias is the effect of a large sea salt coarse mode on fine-mode semi-volatile species. For example, during nighttime, when HNO_3 concentrations are much lower relative to daytime, ISORROPIA-II may have overestimated NO_3^- due to ignoring the presence of a larger more neutral coarse mode when calculating fine-mode aerosol concentrations assuming equilibrium. Various studies show the typical time for the fine mode to reach thermodynamic equilibrium is on the order of 20 min (Dassios and Pandis, 1999; Fountoukis et al., 2009), whereas timescales for the coarse mode to equilibrate are much larger. The mixing of fine particles with high concentrations of coarse mode, mainly sea salt, particles could disrupt fine-mode equilibrium by the mass transfer of volatile fine-mode NO_3^-, via HNO_3, to the coarse mode, forming non-volatile salts, such as $NaNO_3$. This mechanism is consistent with the presence of high levels of sea salt in the LA region and the anti-correlation of a NO_3^- prediction bias with HNO_3 concentration (Fig. S5). During the daytime, when HNO_3 concentrations are high, this bias would be minimal, but at night, when HNO_3 concentrations are low, the model, which ignores the presence of the coarse mode, would overpredict NO_3^- concentrations by not considering fine-mode nitrate loss to the coarse mode. Again, partitioning of NH_3–NH_4^+ would not be affected as much by this process since some fraction of the NH_4^+ would be associated with SO_4^{2-}. Of the various locations where we have investigated pH, this study has the highest coarse-mode inorganic aerosol concentrations (Sardar et al., 2005, report levels of $\sim 20\,\mu g\,m^{-3}$ year round) and is the only one where we have observed this bias (not observed in the eastern US reported by Guo et al., 2016).

4.2 Why is nitrate much higher in LA compared to other regions investigated?

A comparison of pH and related statistics in five field studies is summarized in Table 2. The campaigns are CalNex, SOAS, SENEX, and WINTER, all conducted in the continental US. Also included are results from a study in the eastern Mediterranean (the campaign acronyms are given in Table 2). The SOAS (ground-based) and SENEX (aircraft-based) studies provide an interesting contrast with CalNex, that is, between the southeastern and southwestern US in summertime. WINTER aircraft data add the dimension of seasonal variation (summer versus winter). The eastern Mediterranean data provide a remote European (Crete) and urban (Athens) perspective, and a case where air masses were known to be impacted by biomass burning (BB). All pH values in Table 2 were calculated by ISORROPIA-II in forward metastable mode, but only the US data (SOAS, WINTER, CalNex) used gas–particle phase partitioning to constrain and verify the pH prediction for all the data analyzed. Lack of NH_3 or HNO_3 data for the eastern Mediterranean means that pH was likely underestimated by ~ 0.5 units (Bougiatioti et al., 2016). This was verified with a limited set of data when both aerosol and gas-phase data were available. It is noteworthy that, in all studies, pH was low and on average below 3. The eastern US regions are characterized with the lowest pH (~ 1) throughout the year, from ground level up to 5 km aloft (Guo et al., 2015, 2016; Xu et al., 2016). The highest pH of 2.8 ± 0.6 was consistently observed in biomass-burning-impacted air masses, regardless of season in both the remote and urban eastern Mediterranean and attributed to an abundance of NH_3 and fine particle K^+ in biomass burning emissions, which raised pH and NO_3^- concentrations significantly (Bougiatioti et al., 2017). Biomass burning also accounted for the high pH, which approaches 3, in Athens during winter.

Comparing LA (CalNex) to the other summertime measurements in the eastern US (SOAS, SENEX), Table 2 shows that the LA ground site had uniquely higher NO_3^- and HNO_3 mass concentrations and NO_3^- was the most abundant (by mass) inorganic ion for PM_1 or $PM_{2.5}$. In contrast, in the southeastern US in summertime, SO_4^{2-} was the dominant ion, NO_3^- was only 5–14 % of the SO_4^{2-} mass. The higher total NO_3^- ($NO_3^- + HNO_3$) in LA indicates high local NO_x relative to SO_2 sources. LA also had roughly 1 unit higher PM_1 pH, and much higher NO_3^- concentrations relative to SO_4^{2-}. (Total ammonia ($NH_3 + NH_4^+$) was also higher, Table 2.) The ratio of total NO_3^- and SO_4^{2-} (sulfate is non-volatile, so total sulfate is equivalent to sulfate) was ~ 4 for CalNex, compared to 0.3 for SOAS and 0.8 for SENEX. The higher ratio of total NO_3^- to SO_4^{2-} can explain the higher LA pH through coupling of particle composition, hygroscopicity, and acidity. Consider the situation where there is initially a high HNO_3 concentration. Some HNO_3 will condense onto very acidic particles (e.g., even at low $\varepsilon(NO_3^-)$, with very

Table 2. Comparisons between different studies for particle pH, major inorganic ions and gases and meteorological conditions. All pH values are from ISORROPIA-II run in forward mode. The campaign acronyms other than CalNex stand for Southern Oxidant and Aerosol Study (SOAS), Southeastern Nexus of Air Quality and Climate (SENEX), and Wintertime Investigation of Transport, Emissions, and Reactivity (WINTER).

Campaign	CalNex		SOAS	SENEX[c]	WINTER	Studies in the eastern Mediterranean		
Type	Ground	Ground	Ground	Aircraft	Aircraft	Ground	Ground	(BB plumes)[g]
PM cut size	PM_1	$PM_{2.5}$[a]	PM_1 & $PM_{2.5}$[b]	PM_1	PM_1	PM_1	PM_1	PM_1
Year	2010		2013	2013	2015	2012	2013–2014	2012–2014
Season	(Early) Summer		Summer	Summer	Winter	Summer–autumn	Winter	Summer–winter
Region/location	SW US		SE US	SE US	NE US	Crete, Greece	Athens, Greece	Crete and Athens
SO_4^{2-}, $\mu g\,m^{-3}$	2.86 ± 1.70	1.88 ± 0.69	1.73 ± 1.21	2.05 ± 0.80	1.02 ± 0.77	2.31 ± 1.61	2.31 ± 1.32	1.66 ± 1.49
NO_3^-, $\mu g\,m^{-3}$	3.58 ± 3.65	3.74 ± 1.53	0.08 ± 0.08	0.28 ± 0.09	0.80 ± 1.03	0.12 ± 0.07	2.21 ± 2.02	1.79 ± 1.49
HNO_3, $\mu g\,m^{-3}$	6.65 ± 7.03	4.45 ± 3.59	0.36 ± 0.14	1.35 ± 0.66	1.41 ± 1.83	–	–	0.91 ± 0.39
$\varepsilon(NO_3^-)$	$39 \pm 16\,\%$	$51 \pm 18\,\%$	$22 \pm 16\,\%$	$18 \pm 6\,\%$	$37 \pm 28\,\%$	$< 20\,\%$[e]	–	$65 \pm 14\,\%$
Total NO_3^-, $\mu g\,m^{-3}$	10.22 ± 9.74	8.19 ± 3.89	0.45 ± 0.26	1.63 ± 0.70	2.21 ± 2.21	–	–	3.36 ± 2.08
NH_4^+, $\mu g\,m^{-3}$	2.06 ± 1.67	1.79 ± 0.65	0.46 ± 0.34	1.06 ± 0.25	0.50 ± 0.43	0.81 ± 0.58	1.96 ± 1.30	1.02 ± 0.93
NH_3, $\mu g\,m^{-3}$	1.37 ± 0.90	0.75 ± 0.61	0.39 ± 0.25	0.12 ± 0.19	–	–	–	–
$\varepsilon(NH_4^+)$	$55 \pm 25\,\%$	$71 \pm 19\,\%$	$50 \pm 25\,\%$	$92 \pm 11\,\%$	–	–	–	–
Total NH_4^+, $\mu g\,m^{-3}$	3.44 ± 1.81	2.54 ± 0.89	0.78 ± 0.50	1.17 ± 0.81	–	–	–	–
Na^+, $\mu g\,m^{-3}$	–	0.77 ± 0.39	0.03 ± 0.07	–	0.23 ± 0.46[d]	0.19 ± 0.43	0.13 ± 0.11	0.08 ± 0.05
Cl^-, $\mu g\,m^{-3}$	–	0.64 ± 0.48	0.02 ± 0.03	–	0.34 ± 0.38[d]	0.22 ± 0.53	0.14 ± 0.19	0.20 ± 0.19
RH, %	79 ± 17	87 ± 9	74 ± 16	72 ± 9	58 ± 19	57 ± 11	80 ± 9	68 ± 16
T, °C	18 ± 4	18 ± 3	25 ± 3	22 ± 3	0 ± 8	27 ± 3	12 ± 3	20 ± 9
pH	1.9 ± 0.5	2.7 ± 0.3	0.9 ± 0.6	1.1 ± 0.4	0.8 ± 1.0	1.3 ± 1.1	2.4 ± 0.8	2.8 ± 0.6
Reference	This study		Guo et al. (2015)	Xu et al. (2016)	Guo et al. (2016)	Bougiatioti et al. (2016)	Bougiatioti[f]	Bougiatioti et al. (2016, [f])

[a] Only the last week of CalNex. [b] $PM_{2.5}$ was sampled in the first half and PM_1 sampled in the second half of the study; various parameters were similar in both cases, crustal components were higher, but overall generally low so differences had minor effects, e.g., $PM_{2.5}$ Na^+ was 0.06 ± 0.09 and PM_1 Na^+ was $0.01 \pm 0.01\,\mu g\,m^{-3}$. [c] Only one flight (16 June 2013) statistic from the reference is shown. [d] Externally mixed, thus not included in pH calculation; [e] Estimated from offline measurement. [f] A. Bougiatioti, personal communication, 2016. [g] Averaged from identified biomass burning (BB) plumes from Crete and Athens studies due to the similar pH; K^+ was $0.36 \pm 0.38\,\mu g\,m^{-3}$.

high HNO_3, some NO_3^- can form). If this NO_3^- is significant relative to SO_4^{2-}, it substantially increases the particle W_i, which dilutes the H^+ and raises the pH, since NO_3^- has a similarly high hygroscopicity as SO_4^{2-} (Nenes et al., 1998). Higher pH leads to more NO_3^- formed. This positive feedback, which reaches equilibrium at some point, and along with the condition of higher abundance of NH_3 compared to the southeast (Table 2), may explain the higher NO_3^- and one unit higher pH in LA. This feedback process only happens for semi-volatile highly hygroscopic species. Sulfate will not have this effect since it is non-volatile. It also can only happen when the semi-volatile species contributes a large fraction to the particle W_i, and hence high total NO_3^- to SO_4^{2-} ratios, which is why the effect is not seen in the eastern US in summertime.

To better understand the relationship between NO_3^-, pH, and T across different campaigns, S curves calculated from solubility and dissociation of a species in water, with activity coefficients included, provide a useful conceptual means for comparing pH predictions from the thermodynamic model to measurements of semi-volatile species partitioning between gas–particle phases (see Fig. 5). The intercomparison between the various campaigns is shown in Fig. 8. For each campaign, data are selected within a narrow range (see Fig. 8 caption) to limit the effects of W_i and T variations on gas–particle partitioning. (CalNex $PM_{2.5}$ pH is not included in Fig. 8 due to very limited points since CalNex $PM_{2.5}$ W_i was much higher due to high inorganic mass loadings and an average RH of 87 %.) S curves are calculated based on a W_i of $2.5\,\mu g\,m^{-3}$ and T of 0 and 20 °C for wintertime or summertime conditions, respectively. ISORROPIA-II predicted activity coefficient of the H^+–NO_3^- ion pair, $\gamma_{H^+-NO_3^-}$, is included to account for aqueous solution non-ideality.

Consider the nitrate partitioning case, $\varepsilon(NO_3^-)$, comparing SOAS to WINTER (Fig. 8a versus 8b). Although the data pH ranges are similar in these studies (on average ~ 1), there is higher $\varepsilon(NO_3^-)$ in winter ($T = 0\,°C$) due to the S curve shifting to lower pH (~ 1 unit) relative to summer ($T = 20\,°C$), illustrating the effect of T (which is mainly through HNO_3 Henry's law constant sensitivity to T). Considering only Fig. 8b, as noted above, the temperature ranges were more similar for the SOAS, SENEX, and CalNex studies, yet CalNex had higher particle pH (PM_1) and more nitrate compared

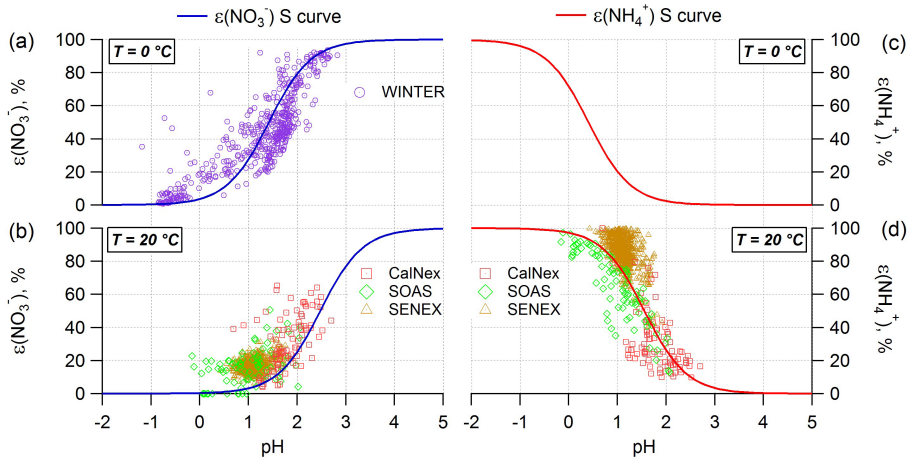

Figure 8. Analytically calculated S curves of $\varepsilon(NO_3^-)$ and $\varepsilon(NH_4^+)$ and ambient data, plotted with ISORROPIA-predicted pH for CalNex, SOAS, SENEX, and WINTER studies. $\varepsilon(NO_3^-)$ and $\varepsilon(NH_4^+)$ are the fraction of the total (gas + particle) in the particle phase. For the data, a narrow range in W_i(1–4 µg m^{-3}) and T ($-5 < T < 5$ °C for $T = 0$ °C, $15 < T < 25$ °C for $T = 20$ °C) data were selected to be close to the analytical calculation input (i.e., $W_i = 2.5$ µg m^{-3} and various T). For analytical calculations (S curves), $\gamma_{NH_4^+} = 1$ was applied; ISORROPIA-II predicted $\gamma_{H^+-NO_3^-}$ 0.23 (WINTER) and 0.28 (CalNex 0.28, SOAS 0.29, SENEX 0.26) were used.

to SOAS and SENEX due to higher total NO_3 relative to SO_4^{2-}, which leads to more nitrate formation through feedbacks involving particle water and pH, as discussed above. This can also be seen in Fig. 8b.

$\varepsilon(NH_4^+)$ S curves and data from the field studies are shown in Fig. 8c and d. Note that the $\varepsilon(NO_3^-)$ and $\varepsilon(NH_4^+)$ face opposite directions since it is acid versus base. NH_3 data were not available during WINTER so no measured $\varepsilon(NH_4^+)$ points were plotted at 0 °C and no comparisons as a function of T can be made. At 20 °C, the $\varepsilon(NH_4^+)$ of CalNex, SOAS, and SENEX all converge around one S curve, which was calculated assuming $\gamma_{H^+-NH_4^+} = 1$. The lower pH of SOAS and SENEX relative to CalNex resulted in generally higher $\varepsilon(NH_4^+)$, and more ammonia partitioned to the particle phase. The data and predicted $\varepsilon(NH_4^+)$ are in fairly good agreement.

S curves have significant utility for understanding how T, RH, and pH affect partitioning (e.g., see Fig. S3 and S4), but we also note that they can be used to estimate activity coefficients based on partitioning data, which may be particularly useful in situations where the data are not available from the literature (e.g., organic acids above a mixture of inorganic and organics).

5 Summary

pH of PM_1 and $PM_{2.5}$ and the semi-volatile gas–particle partitioning of HNO_3–NO_3^-, NH_3–NH_4^+, and HCl–Cl^- in the LA Basin during the 2010 CalNex study were investigated. As a coastal urban site impacted by high sea salt aerosol components and high total nitrate (HNO_3+NO_3^-) and ammonia levels, this study provided a contrast to pH we have reported in the eastern US and eastern Mediterranean.

PM_1 single-particle analysis showed that 73 % (by number) of PM_1 sea salt particles did not contain nitrate and sea salt type particles only contributed to 12 % to PM_1 mass. Therefore, PM_1 pH was predicted solely on the SO_4^{2-}–NO_3^-–NH_4^+–HNO_3–NH_3 system (ISORROPIA-II inputs). This approach provided good agreement between observed and model-predicted partitioning of NH_3–NH_4^+ and HNO_3–NO_3^-, although a bias in $\varepsilon(NO_3^-)$ was observed that depended on RH (day vs. night). Altering gas and particle temperatures from ambient due to the sampling configurations did not explain the bias. A likely cause is the loss of fine-mode NO_3^- to coarse-mode sea salt, mainly at night, when HNO_3 concentrations are low, which is not considered by the thermodynamic model used to predict fine-mode concentrations.

The study mean (±SD) PM_1 pH in the LA Basin was 1.9 ± 0.5, roughly one unit higher than the average pH observed in summer in the southeastern US (0.9 ± 0.6 and 1.1 ± 0.4), despite similar RH and T ranges and both calculated for the SO_4^{2-}–NO_3^-–NH_4^+–HNO_3–NH_3 system. The cause may be much higher total nitrate concentrations (high NO_x and proximity to locations of HNO_3 formation) relative to sulfate in LA. For example, high levels of HNO_3 can lead to at least some particulate NO_3^-, even if conditions are such that NO_3^- partitioning is low (e.g., $\varepsilon(NO_3^-)$ is small). NO_3^- increases the particle water, which raises pH by dilution of H^+, allowing more partitioning (i.e., increases $\varepsilon(NO_3^-)$). When non-volatile sulfate dominates over total nitrate, sulfate controls liquid water and this effect is not observed. The

complex interactions between pH, LWC, T, and NO_3^- are clearly illustrated by analytical ("S" curve) analyses.

Single-particle analysis showed that 85 % by number of sea salt particles in the 1 to 2.5 µm nominal range contained nitrate and that the model-predicted partitioning of HNO_3–NO_3^- for $PM_{2.5}$ agreed better with the observed partitioning when sea salt components were included (SO_4^{2-}–NO_3^-–NH_4^+–Na^+–Cl^-–K^+–HNO_3–NH_3–HCl system). Bulk $PM_{2.5}$ pH was 2.7 ± 0.3, whereas for the same time period PM_1 pH was 1.9 ± 0.4 and the diurnal pH profiles of PM_1 and $PM_{2.5}$ also differed, all apparently due to the influence of sea salt aerosols.

The CalNex data provide unique contrast to pH reported in other regions and demonstrates the complex interactions between pH and emissions. They also support the general application of SO_4^{2-}–NO_3^-–NH_4^+–HNO_3–NH_3 system for predictions of PM_1 pH and gas–particle phase partitioning without considering sea salts or crustal elements, useful for regional or global modeling. They further illustrate that fine particles have surprisingly low pH in many locations, which has significant effects on the many environmental impacts of fine particles.

Data availability. The data were collected during the 2010 CalNex ground campaign in LA and open to the public at the NOAA website, https://esrl.noaa.gov/csd/groups/csd7/measurements/2010calnex/Ground/DataDownload/ (NOAA, 2016). The particle pH data are accessible by contacting the corresponding authors.

The Supplement related to this article is available online at doi:10.5194/acp-17-5703-2017-supplement.

Competing interests. The authors declare that they have no conflict of interest.

Acknowledgements. The Georgia Tech researchers were funded through National Science Foundation (NSF) grants AGS-0931492 and AGS-0802237. This work was also supported by the NSF under grants AGS-1242258 and AGS-1360730, which supported our participation in the SOAS and WINTER campaigns. We wish to thank Aikaterini Bougiatioti for sharing the eastern Mediterranean data included in Table 2 and Raluca Ellis and Jennifer Murphy for use of the gas-phase ammonia data. P. L. Hayes and J. L. Jimenez were partially supported by NSF grant AGS-1360834. We thank Amber Ortega for providing the residence time in the AMS inlet. The NOAA work was supported by the NOAA Air Quality and Climate Research programs.

Edited by: A. Kiendler-Scharr
Reviewed by: two anonymous referees

References

Ansari, A. S. and Pandis, S. N.: The effect of metastable equilibrium states on the partitioning of nitrate between the gas and aerosol phases, Atmos. Environ., 34, 157–168, doi:10.1016/s1352-2310(99)00242-3, 2000.

Bertram, A. K., Martin, S. T., Hanna, S. J., Smith, M. L., Bodsworth, A., Chen, Q., Kuwata, M., Liu, A., You, Y., and Zorn, S. R.: Predicting the relative humidities of liquid-liquid phase separation, efflorescence, and deliquescence of mixed particles of ammonium sulfate, organic material, and water using the organic-to-sulfate mass ratio of the particle and the oxygen-to-carbon elemental ratio of the organic component, Atmos. Chem. Phys., 11, 10995–11006, doi:10.5194/acp-11-10995-2011, 2011.

Bougiatioti, A., Nikolaou, P., Stavroulas, I., Kouvarakis, G., Weber, R., Nenes, A., Kanakidou, M., and Mihalopoulos, N.: Particle water and pH in the eastern Mediterranean: source variability and implications for nutrient availability, Atmos. Chem. Phys., 16, 4579–4591, doi:10.5194/acp-16-4579-2016, 2016.

Clegg, S. L., Brimblecombe, P., and Wexler, A. S.: Thermodynamic model of the system H^+-NH_4^+-SO_4^{2-}-NO_3^--H_2O at tropospheric temperatures, J. Phys. Chem. A, 102, 2137–2154, doi:10.1021/Jp973042r, 1998.

Clegg, S. L., Seinfeld, J. H., and Edney, E. O.: Thermodynamic modelling of aqueous aerosols containing electrolytes and dissolved organic compounds. II. An extended Zdanovskii–Stokes–Robinson approach, J. Aerosol Sci., 34, 667–690, doi:10.1016/s0021-8502(03)00019-3, 2003.

Dassios, K. G. and Pandis, S. N.: The mass accommodation coefficient of ammonium nitrate aerosol, Atmos. Environ., 33, 2993–3003, doi:10.1016/S1352-2310(99)00079-5, 1999.

DeCarlo, P. F., Kimmel, J. R., Trimborn, A., Northway, M. J., Jayne, J. T., Aiken, A. C., Gonin, M., Fuhrer, K., Horvath, T., Docherty, K. S., Worsnop, D. R., and Jimenez, J. L.: Field-deployable, high-resolution, time-of-flight aerosol mass spectrometer, Anal. Chem., 78, 8281–8289, doi:10.1021/ac061249n, 2006.

Dockery, D. W., Cunningham, J., Damokosh, A. I., Neas, L. M., Spengler, J. D., Koutrakis, P., Ware, J. H., Raizenne, M., and Speizer, F. E.: Health effects of acid aerosols on North American children: respiratory symptoms, Environ. Health Persp., 104, 500–505, 1996.

Duce, R. A. and Tindale, N. W.: Atmospheric transport of iron and its deposition in the ocean, Limnol. Oceanogr., 36, 1715–1726, doi:10.4319/lo.1991.36.8.1715, 1991.

Duyzer, J.: Dry deposition of ammonia and ammonium aerosols over heathland, J. Geophys. Res.-Atmos., 99, 18757–18763, doi:10.1029/94jd01210, 1994.

Eddingsaas, N. C., VanderVelde, D. G., and Wennberg, P. O.: Kinetics and Products of the Acid-Catalyzed Ring-Opening of Atmospherically Relevant Butyl Epoxy Alcohols, J. Phys. Chem. A, 114, 8106–8113, doi:10.1021/Jp103907c, 2010.

Edney, E. O., Kleindienst, T. E., Jaoui, M., Lewandowski, M., Offenberg, J. H., Wang, W., and Claeys, M.: Formation of 2-methyl tetrols and 2-methylglyceric acid in secondary organic aerosol from laboratory irradiated isoprene / NO_X / SO_2 / air mixtures and their detection in ambient $PM_{2.5}$ samples collected in the eastern United States, Atmos. Environ., 39, 5281–5289, doi:10.1016/j.atmosenv.2005.05.031, 2005.

Ellis, R. A., Murphy, J. G., Pattey, E., van Haarlem, R., O'Brien, J. M., and Herndon, S. C.: Characterizing a Quantum Cascade Tunable Infrared Laser Differential Absorption Spectrometer (QC-TILDAS) for measurements of atmospheric ammonia, Atmos. Meas. Tech., 3, 397–406, doi:10.5194/amt-3-397-2010, 2010.

Enami, S., Hoffmann, M. R., and Colussi, A. J.: Acidity enhances the formation of a persistent ozonide at aqueous ascorbate/ozone gas interfaces, P. Natl. Acad. Sci. USA, 105, 7365–7369, doi:10.1073/pnas.0710791105, 2008.

Fang, T., Guo, H., Verma, V., Peltier, R. E., and Weber, R. J.: $PM_{2.5}$ water-soluble elements in the southeastern United States: automated analytical method development, spatiotemporal distributions, source apportionment, and implications for heath studies, Atmos. Chem. Phys., 15, 11667–11682, doi:10.5194/acp-15-11667-2015, 2015.

Fang, T., Guo, H., Zeng, L., Verma, V., Nenes, A., and Weber, R. J.: Highly acidic ambient particles, soluble metals and oxidative potential: A link between sulfate and aerosol toxicity, Environ. Sci. Technol., 51, 2611–2620, doi:10.1021/acs.est.6b06151, 2017.

Fountoukis, C. and Nenes, A.: ISORROPIA II: a computationally efficient thermodynamic equilibrium model for K^+-Ca^{2+}-Mg^{2+}-NH_4^+-Na^+-SO_4^{2-}-NO_3^--Cl^--H_2O aerosols, Atmos. Chem. Phys., 7, 4639–4659, doi:10.5194/acp-7-4639-2007, 2007.

Fountoukis, C., Nenes, A., Sullivan, A., Weber, R., Van Reken, T., Fischer, M., Matias, E., Moya, M., Farmer, D., and Cohen, R. C.: Thermodynamic characterization of Mexico City aerosol during MILAGRO 2006, Atmospheric Chemistry and Physics, 9, 2141–2156, doi:10.5194/acp-9-2141-2009, 2009.

Froyd, K. D., Murphy, D. M., Lawson, P., Baumgardner, D., and Herman, R. L.: Aerosols that form subvisible cirrus at the tropical tropopause, Atmos. Chem. Phys., 10, 209–218, doi:10.5194/acp-10-209-2010, 2010.

Gao, S., Keywood, M., Ng, N. L., Surratt, J., Varutbangkul, V., Bahreini, R., Flagan, R. C., and Seinfeld, J. H.: Low-molecular-weight and oligomeric components in secondary organic aerosol from the ozonolysis of cycloalkenes and a-pinene, J. Phys. Chem. A, 108, 10147–10164, doi:10.1021/Jp047466e, 2004.

Ghio, A. J., Carraway, M. S., and Madden, M. C.: Composition of air pollution particles and oxidative stress in cells, tissues, and living systems, J. Toxicol. Env. Heal. B,, 15, 1–21, doi:10.1080/10937404.2012.632359, 2012.

Guo, H., Xu, L., Bougiatioti, A., Cerully, K. M., Capps, S. L., Hite Jr., J. R., Carlton, A. G., Lee, S.-H., Bergin, M. H., Ng, N. L., Nenes, A., and Weber, R. J.: Fine-particle water and pH in the southeastern United States, Atmos. Chem. Phys., 15, 5211–5228, doi:10.5194/acp-15-5211-2015, 2015.

Guo, H., Sullivan, A. P., Campuzano-Jost, P., Schroder, J. C., Lopez-Hilfiker, F. D., Dibb, J. E., Jimenez, J. L., Thornton, J. A., Brown, S. S., Nenes, A., and Weber, R. J.: Fine particle pH and the partitioning of nitric acid during winter in the northeastern United States, J. Geophys. Res.-Atmos., 121, 10355–10376, doi:10.1002/2016jd025311, 2016.

Gwynn, R. C., Burnett, R. T., and Thurston, G. D.: A time-series analysis of acidic particulate matter and daily mortality and morbidity in the Buffalo, New York, region, Environ. Health Persp., 108, 125–133, 2000.

Han, Y., Stroud, C. A., Liggio, J., and Li, S.-M.: The effect of particle acidity on secondary organic aerosol formation from a-pinene photooxidation under atmospherically relevant conditions, Atmos. Chem. Phys., 16, 13929–13944, doi:10.5194/acp-16-13929-2016, 2016.

Hand, J. L., Schichtel, B. A., Pitchford, M., Malm, W. C., and Frank, N. H.: Seasonal composition of remote and urban fine particulate matter in the United States, J. Geophys. Res.-Atmos., 117, D05209, doi:10.1029/2011jd017122, 2012.

Hayes, P. L., Ortega, A. M., Cubison, M. J., Froyd, K. D., Zhao, Y., Cliff, S. S., Hu, W. W., Toohey, D. W., Flynn, J. H., Lefer, B. L., Grossberg, N., Alvarez, S., Rappenglück, B., Taylor, J. W., Allan, J. D., Holloway, J. S., Gilman, J. B., Kuster, W. C., de Gouw, J. A., Massoli, P., Zhang, X., Liu, J., Weber, R. J., Corrigan, A. L., Russell, L. M., Isaacman, G., Worton, D. R., Kreisberg, N. M., Goldstein, A. H., Thalman, R., Waxman, E. M., Volkamer, R., Lin, Y. H., Surratt, J. D., Kleindienst, T. E., Offenberg, J. H., Dusanter, S., Griffith, S., Stevens, P. S., Brioude, J., Angevine, W. M., and Jimenez, J. L.: Organic aerosol composition and sources in Pasadena, California, during the 2010 CalNex campaign, J. Geophys. Res.-Atmos., 118, 9233–9257, doi:10.1002/jgrd.50530, 2013.

Hayes, P. L., Carlton, A. G., Baker, K. R., Ahmadov, R., Washenfelder, R. A., Alvarez, S., Rappenglück, B., Gilman, J. B., Kuster, W. C., de Gouw, J. A., Zotter, P., Prévôt, A. S. H., Szidat, S., Kleindienst, T. E., Offenberg, J. H., Ma, P. K., and Jimenez, J. L.: Modeling the formation and aging of secondary organic aerosols in Los Angeles during CalNex 2010, Atmos. Chem. Phys., 15, 5773–5801, doi:10.5194/acp-15-5773-2015, 2015.

Hennigan, C. J., Sandholm, S., Kim, S., Stickel, R. E., Huey, L. G., and Weber, R. J.: Influence of Ohio River valley emissions on fine particle sulfate measured from aircraft over large regions of the eastern United States and Canada during INTEX-NA, J. Geophys. Res.-Atmos., 111, D24S04, doi:10.1029/2006Jd007282, 2006.

Hennigan, C. J., Sullivan, A. P., Fountoukis, C. I., Nenes, A., Hecobian, A., Vargas, O., Peltier, R. E., Case Hanks, A. T., Huey, L. G., Lefer, B. L., Russell, A. G., and Weber, R. J.: On the volatility and production mechanisms of newly formed nitrate and water soluble organic aerosol in Mexico City, Atmos. Chem. Phys., 8, 3761–3768, doi:10.5194/acp-8-3761-2008, 2008.

Hennigan, C. J., Izumi, J., Sullivan, A. P., Weber, R. J., and Nenes, A.: A critical evaluation of proxy methods used to estimate the acidity of atmospheric particles, Atmos. Chem. Phys., 15, 2775–2790, doi:10.5194/acp-15-2775-2015, 2015.

Huebert, B. J. and Robert, C. H.: The Dry Deposition of Nitric-Acid to Grass, J. Geophys. Res.-Atmos., 90, 2085–2090, doi:10.1029/JD090iD01p02085, 1985.

Huffman, J. A., Docherty, K. S., Aiken, A. C., Cubison, M. J., Ulbrich, I. M., DeCarlo, P. F., Sueper, D., Jayne, J. T., Worsnop, D. R., Ziemann, P. J., and Jimenez, J. L.: Chemically-resolved aerosol volatility measurements from two megacity field studies, Atmos. Chem. Phys., 9, 7161–7182, doi:10.5194/acp-9-7161-2009, 2009.

IPCC: Climate Change 2013: The Physical Science Basis. Working Group I Contribution to the Fifth Assessment Report of the International Panel on Climate Change., Cambridge, United Kingdom and New York, NY, USA, 1535, 2013.

Ito, A. and Xu, L.: Response of acid mobilization of iron-containing mineral dust to improvement of air quality projected in the future,

Atmos. Chem. Phys., 14, 3441–3459, doi:10.5194/acp-14-3441-2014, 2014.

Ito, T., Nenes, A., Johnson, M. S., Meskhidze, N., and Deutsch, C.: Acceleration of oxygen decline in the tropical Pacific over the past decades by aerosol pollutants, Nat. Geosci., 9, 443–447, doi:10.1038/ngeo2717, 2016.

Jang, M., Czoschke, N. M., Lee, S., and Kamens, R. M.: Heterogeneous atmospheric aerosol production by acid-catalyzed particle-phase reactions, Science, 298, 814–817, doi:10.1126/science.1075798, 2002.

Koutrakis, P., Wolfson, J. M., and Spengler, J. D.: An improved method for measuring aerosol strong acidity: Results from a nine-month study in St Louis, Missouri and Kingston, Tennessee, Atmos. Environ., 22, 157–162, doi:10.1016/0004-6981(88)90308-3, 1988.

Langer, S., Pemberton, R. S., and Finlayson-Pitts, B. J.: Diffuse Reflectance Infrared Studies of the Reaction of Synthetic Sea Salt Mixtures with NO_2: A Key Role for Hydrates in the Kinetics and Mechanism, J. Phys. Chem. A, 101, 1277–1286, doi:10.1021/jp962122c, 1997.

Last, J. A.: Global atmospheric change: potential health effects of acid aerosol and oxidant gas mixtures, Environ. Health Persp., 96, 151–157, doi:10.1289/ehp.9196151, 1991.

Lelieveld, J., Evans, J. S., Fnais, M., Giannadaki, D., and Pozzer, A.: The contribution of outdoor air pollution sources to premature mortality on a global scale, Nature, 525, 367–371, doi:10.1038/nature15371, 2015.

Li, W., Xu, L., Liu, X., Zhang, J., Lin, Y., Yao, X., Gao, H., Zhang, D., Chen, J., Wang, W., Harrison, R. M., Zhang, X., Shao, L., Fu, P., Nenes, A., and Shi, Z.: Air pollution-aerosol interactions produce more bioavailable iron for ocean ecosystems, Sci. Adv., 3, e1601749, doi:10.1126/sciadv.1601749, 2017.

Lim, S. S., Vos, T., Flaxman, A. D., Danaei, G., Shibuya, K., Adair-Rohani, H., AlMazroa, M. A., Amann, M., Anderson, H. R., Andrews, K. G., Aryee, M., Atkinson, C., Bacchus, L. J., Bahalim, A. N., Balakrishnan, K., Balmes, J., Barker-Collo, S., Baxter, A., Bell, M. L., Blore, J. D., Blyth, F., Bonner, C., Borges, G., Bourne, R., Boussinesq, M., Brauer, M., Brooks, P., Bruce, N. G., Brunekreef, B., Bryan-Hancock, C., Bucello, C., Buchbinder, R., Bull, F., Burnett, R. T., Byers, T. E., Calabria, B., Carapetis, J., Carnahan, E., Chafe, Z., Charlson, F., Chen, H., Chen, J. S., Cheng, A. T.-A., Child, J. C., Cohen, A., Colson, K. E., Cowie, B. C., Darby, S., Darling, S., Davis, A., Degenhardt, L., Dentener, F., Des Jarlais, D. C., Devries, K., Dherani, M., Ding, E. L., Dorsey, E. R., Driscoll, T., Edmond, K., Ali, S. E., Engell, R. E., Erwin, P. J., Fahimi, S., Falder, G., Farzadfar, F., Ferrari, A., Finucane, M. M., Flaxman, S., Fowkes, F. G. R., Freedman, G., Freeman, M. K., Gakidou, E., Ghosh, S., Giovannucci, E., Gmel, G., Graham, K., Grainger, R., Grant, B., Gunnell, D., Gutierrez, H. R., Hall, W., Hoek, H. W., Hogan, A., Hosgood Iii, H. D., Hoy, D., Hu, H., Hubbell, B. J., Hutchings, S. J., Ibeanusi, S. E., Jacklyn, G. L., Jasrasaria, R., Jonas, J. B., Kan, H., Kanis, J. A., Kassebaum, N., Kawakami, N., Khang, Y.-H., Khatibzadeh, S., Khoo, J.-P., Kok, C., Laden, F., Lalloo, R., Lan, Q., Lathlean, T., Leasher, J. L., Leigh, J., Li, Y., Lin, J. K., Lipshultz, S. E., London, S., Lozano, R., Lu, Y., Mak, J., Malekzadeh, R., Mallinger, L., Marcenes, W., March, L., Marks, R., Martin, R., McGale, P., McGrath, J., Mehta, S., Memish, Z. A., Mensah, G. A., Merriman, T. R., Micha, R., Michaud, C., Mishra, V., Hanafiah, K. M., Mokdad, A. A., Morawska, L., Mozaffarian, D., Murphy, T., Naghavi, M., Neal, B., Nelson, P. K., Nolla, J. M., Norman, R., Olives, C., Omer, S. B., Orchard, J., Osborne, R., Ostro, B., Page, A., Pandey, K. D., Parry, C. D. H., Passmore, E., Patra, J., Pearce, N., Pelizzari, P. M., Petzold, M., Phillips, M. R., Pope, D., Pope Iii, C. A., Powles, J., Rao, M., Razavi, H., Rehfuess, E. A., Rehm, J. T., Ritz, B., Rivara, F. P., Roberts, T., Robinson, C., Rodriguez-Portales, J. A., Romieu, I., Room, R., Rosenfeld, L. C., Roy, A., Rushton, L., Salomon, J. A., Sampson, U., Sanchez-Riera, L., Sanman, E., Sapkota, A., Seedat, S., Shi, P., Shield, K., Shivakoti, R., Singh, G. M., Sleet, D. A., Smith, E., Smith, K. R., Stapelberg, N. J. C., Steenland, K., Stöckl, H., Stovner, L. J., Straif, K., Straney, L., Thurston, G. D., Tran, J. H., Van Dingenen, R., van Donkelaar, A., Veerman, J. L., Vijayakumar, L., Weintraub, R., Weissman, M. M., White, R. A., Whiteford, H., Wiersma, S. T., Wilkinson, J. D., Williams, H. C., Williams, W., Wilson, N., Woolf, A. D., Yip, P., Zielinski, J. M., Lopez, A. D., Murray, C. J. L., and Ezzati, M.: A comparative risk assessment of burden of disease and injury attributable to 67 risk factors and risk factor clusters in 21 regions, 1990–2010: a systematic analysis for the Global Burden of Disease Study 2010, The Lancet, 380, 2224–2260, doi:10.1016/S0140-6736(12)61766-8, 2012.

Liu, J., Zhang, X., Parker, E. T., Veres, P. R., Roberts, J. M., de Gouw, J. A., Hayes, P. L., Jimenez, J. L., Murphy, J. G., Ellis, R. A., Huey, L. G., and Weber, R. J.: On the gas-particle partitioning of soluble organic aerosol in two urban atmospheres with contrasting emissions: 2. Gas and particle phase formic acid, J. Geophys. Res., 117, D00V21, doi:10.1029/2012jd017912, 2012.

Longo, A. F., Feng, Y., Lai, B., Landing, W. M., Shelley, R. U., Nenes, A., Mihalopoulos, N., Violaki, K., and Ingall, E. D.: Influence of Atmospheric Processes on the Solubility and Composition of Iron in Saharan Dust, Environ. Sci. Technol., 50, 6912–6920, doi:10.1021/acs.est.6b02605, 2016.

Malm, W. C. and Day, D. E.: Estimates of aerosol species scattering characteristics as a function of relative humidity, Atmos. Environ., 35, 2845–2860, doi:10.1016/S1352-2310(01)00077-2, 2001.

Mei, F., Hayes, P. L., Ortega, A., Taylor, J. W., Allan, J. D., Gilman, J., Kuster, W., de Gouw, J., Jimenez, J. L., and Wang, J.: Droplet activation properties of organic aerosols observed at an urban site during CalNex-LA, J. Geophys. Res.-Atmos., 118, 2903–2917, doi:10.1002/jgrd.50285, 2013.

Meskhidze, N., Chameides, W. L., Nenes, A., and Chen, G.: Iron mobilization in mineral dust: Can anthropogenic SO_2 emissions affect ocean productivity?, Geophys. Res. Lett., 30, 2085, doi:10.1029/2003gl018035, 2003.

Middlebrook, A. M., Bahreini, R., Jimenez, J. L., and Canagaratna, M. R.: Evaluation of Composition-Dependent Collection Efficiencies for the Aerodyne Aerosol Mass Spectrometer using Field Data, Aerosol Sci. Tech., 46, 258–271, doi:10.1080/02786826.2011.620041, 2012.

Murphy, D. M., Cziczo, D. J., Froyd, K. D., Hudson, P. K., Matthew, B. M., Middlebrook, A. M., Peltier, R. E., Sullivan, A., Thomson, D. S., and Weber, R. J.: Single-particle mass spectrometry of tropospheric aerosol particles, J. Geophys. Res., 111, D23S32, doi:10.1029/2006jd007340, 2006.

Myriokefalitakis, S., Daskalakis, N., Mihalopoulos, N., Baker, A. R., Nenes, A., and Kanakidou, M.: Changes in dissolved iron deposition to the oceans driven by human activity: a

3-D global modelling study, Biogeosciences, 12, 3973–3992, doi:10.5194/bg-12-3973-2015, 2015.

Nenes, A., Pandis, S. N., and Pilinis, C.: ISORROPIA: A new thermodynamic equilibrium model for multiphase multicomponent inorganic aerosols, Aquat. Geochem., 4, 123–152, doi:10.1023/A:1009604003981, 1998.

Nenes, A., Krom, M. D., Mihalopoulos, N., Van Cappellen, P., Shi, Z., Bougiatioti, A., Zarmpas, P., and Herut, B.: Atmospheric acidification of mineral aerosols: a source of bioavailable phosphorus for the oceans, Atmos. Chem. Phys., 11, 6265–6272, doi:10.5194/acp-11-6265-2011, 2011.

NOAA: The 2010 CalNex LA ground site data, available at: https://esrl.noaa.gov/csd/groups/csd7/measurements/2010calnex/Ground/DataDownload/, 2016.

Oakes, M., Ingall, E. D., Lai, B., Shafer, M. M., Hays, M. D., Liu, Z. G., Russell, A. G., and Weber, R. J.: Iron solubility related to particle sulfur content in source emission and ambient fine particles, Environ. Sci. Technol., 46, 6637–6644, doi:10.1021/es300701c, 2012.

Orsini, D. A., Ma, Y., Sullivan, A., Sierau, B., Baumann, K., and Weber, R. J.: Refinements to the particle-into-liquid sampler (PILS) for ground and airborne measurements of water soluble aerosol composition, Atmos. Environ., 37, 1243–1259, doi:10.1016/s1352-2310(02)01015-4, 2003.

Peltier, R. E., Sullivan, A. P., Weber, R. J., Brock, C. A., Wollny, A. G., Holloway, J. S., de Gouw, J. A., and Warneke, C.: Fine aerosol bulk composition measured on WP-3D research aircraft in vicinity of the Northeastern United States – results from NEAQS, Atmos. Chem. Phys., 7, 3231–3247, doi:10.5194/acp-7-3231-2007, 2007.

Raizenne, M., Neas, L. M., Damokosh, A. I., Dockery, D. W., Spengler, J. D., Koutrakis, P., Ware, J. H., and Speizer, F. E.: Health effects of acid aerosols on North American children: pulmonary function, Environ. Health Persp., 104, 506–514, 1996.

Riipinen, I., Pierce, J. R., Donahue, N. M., and Pandis, S. N.: Equilibration time scales of organic aerosol inside thermodenuders: Evaporation kinetics versus thermodynamics, Atmos. Environ., 44, 597–607, doi:10.1016/j.atmosenv.2009.11.022, 2010.

Robbins, R. C., Cadle, R. D., and Eckhardt, D. L.: The Conversion of Sodium Chloride to Hydrogen Chloride in the Atmosphe, J. Meteorol., 16, 53–56, doi:10.1175/1520-0469(1959)016<0053:tcosct>2.0.co;2, 1959.

Ryerson, T. B., Andrews, A. E., Angevine, W. M., Bates, T. S., Brock, C. A., Cairns, B., Cohen, R. C., Cooper, O. R., de Gouw, J. A., Fehsenfeld, F. C., Ferrare, R. A., Fischer, M. L., Flagan, R. C., Goldstein, A. H., Hair, J. W., Hardesty, R. M., Hostetler, C. A., Jimenez, J. L., Langford, A. O., McCauley, E., McKeen, S. A., Molina, L. T., Nenes, A., Oltmans, S. J., Parrish, D. D., Pederson, J. R., Pierce, R. B., Prather, K., Quinn, P. K., Seinfeld, J. H., Senff, C. J., Sorooshian, A., Stutz, J., Surratt, J. D., Trainer, M., Volkamer, R., Williams, E. J., and Wofsy, S. C.: The 2010 California Research at the Nexus of Air Quality and Climate Change (CalNex) field study, J. Geophys. Res.-Atmos., 118, 5830–5866, doi:10.1002/jgrd.50331, 2013.

Sardar, S. B., Fine, P. M., and Sioutas, C.: Seasonal and spatial variability of the size-resolved chemical composition of particulate matter (PM_{10}) in the Los Angeles Basin, J. Geophys. Res.-Atmos., 110, D07S08, doi:10.1029/2004jd004627, 2005.

Schill, G. P. and Tolbert, M. A.: Heterogeneous ice nucleation on phase-separated organic-sulfate particles: effect of liquid vs. glassy coatings, Atmos. Chem. Phys., 13, 4681–4695, doi:10.5194/acp-13-4681-2013, 2013.

Schrader, F. and Brummer, C.: Land Use Specific Ammonia Deposition Velocities: a Review of Recent Studies (2004–2013), Water, air, and soil pollution, 225, 2114, doi:10.1007/s11270-014-2114-7, 2014.

Song, M., Marcolli, C., Krieger, U. K., Zuend, A., and Peter, T.: Liquid-liquid phase separation and morphology of internally mixed dicarboxylic acids/ammonium sulfate/water particles, Atmos. Chem. Phys., 12, 2691–2712, doi:10.5194/acp-12-2691-2012, 2012.

Sullivan, A. P., Peltier, R. E., Brock, C. A., de Gouw, J. A., Holloway, J. S., Warneke, C., Wollny, A. G., and Weber, R. J.: Airborne measurements of carbonaceous aerosol soluble in water over northeastern United States: Method development and an investigation into water-soluble organic carbon sources, J. Geophys. Res., 111, D23S46, doi:10.1029/2006jd007072, 2006.

Surratt, J. D., Lewandowski, M., Offenberg, J. H., Jaoui, M., Kleindienst, T. E., Edney, E. O., and Seinfeld, J. H.: Effect of acidity on secondary organic aerosol formation from isoprene, Environ. Sci. Technol., 41, 5363–5369, doi:10.1021/es0704176, 2007.

Surratt, J. D., Chan, A. W., Eddingsaas, N. C., Chan, M., Loza, C. L., Kwan, A. J., Hersey, S. P., Flagan, R. C., Wennberg, P. O., and Seinfeld, J. H.: Reactive intermediates revealed in secondary organic aerosol formation from isoprene, P. Natl. Acad. Sci. USA, 107, 6640–6645, doi:10.1073/pnas.0911114107, 2010.

Thurston, G. D., Ito, K., Hayes, C. G., Bates, D. V., and Lippmann, M.: Respiratory hospital admissions and summertime haze air pollution in Toronto, Ontario: consideration of the role of acid aerosols, Environ. Res., 65, 271–290, doi:10.1006/enrs.1994.1037, 1994.

Veres, P., Roberts, J. M., Warneke, C., Welsh-Bon, D., Zahniser, M., Herndon, S., Fall, R., and de Gouw, J.: Development of negative-ion proton-transfer chemical-ionization mass spectrometry (NI-PT-CIMS) for the measurement of gas-phase organic acids in the atmosphere, Int. J. Mass Spectrom., 274, 48–55, doi:10.1016/j.ijms.2008.04.032, 2008.

Veres, P. R., Roberts, J. M., Cochran, A. K., Gilman, J. B., Kuster, W. C., Holloway, J. S., Graus, M., Flynn, J., Lefer, B., Warneke, C., and de Gouw, J.: Evidence of rapid production of organic acids in an urban air mass, Geophys. Res. Lett., 38, L17807, doi:10.1029/2011gl048420, 2011.

Verma, V., Fang, T., Guo, H., King, L., Bates, J. T., Peltier, R. E., Edgerton, E., Russell, A. G., and Weber, R. J.: Reactive oxygen species associated with water-soluble PM2.5 in the southeastern United States: spatiotemporal trends and source apportionment, Atmos. Chem. Phys., 14, 12915–12930, doi:10.5194/acp-14-12915-2014, 2014.

Washenfelder, R. A., Young, C. J., Brown, S. S., Angevine, W. M., Atlas, E. L., Blake, D. R., Bon, D. M., Cubison, M. J., de Gouw, J. A., Dusanter, S., Flynn, J., Gilman, J. B., Graus, M., Griffith, S., Grossberg, N., Hayes, P. L., Jimenez, J. L., Kuster, W. C., Lefer, B. L., Pollack, I. B., Ryerson, T. B., Stark, H., Stevens, P. S., and Trainer, M. K.: The glyoxal budget and its contribution to organic aerosol for Los Angeles, California, during CalNex 2010, J. Geophys. Res.-Atmos., 116, D00V02, doi:10.1029/2011jd016314, 2011.

Weber, R. J., Guo, H., Russell, A. G., and Nenes, A.: High aerosol acidity despite declining atmospheric sulfate concentrations over the past 15 years, Nat. Geosci., 9, 282–285, doi:10.1038/ngeo2665, 2016.

Wexler, A. S. and Clegg, S. L.: Atmospheric aerosol models for systems including the ions H^+, NH_4^+, Na^+, SO_4^{2-}, NO_3^-, Cl^-, Br^-, and H_2O, J. Geophys. Res., 107, 4207, doi:10.1029/2001jd000451, 2002.

Xu, L., Middlebrook, A. M., Liao, J., de Gouw, J. A., Guo, H., Weber, R. J., Nenes, A., Lopez-Hilfiker, F. D., Lee, B. H., Thornton, J. A., Brock, C. A., Neuman, J. A., Nowak, J. B., Pollack, I. B., Welti, A., Graus, M., Warneke, C., and Ng, N. L.: Enhanced formation of isoprene-derived organic aerosol in sulfur-rich power plant plumes during Southeast Nexus, J. Geophys. Res.-Atmos., 121, 11137–111153, doi:10.1002/2016jd025156, 2016.

Ye, Q., Robinson, E. S., Ding, X., Ye, P., Sullivan, R. C., and Donahue, N. M.: Mixing of secondary organic aerosols versus relative humidity, P. Natl. Acad. Sci. USA, 113, 12649–12654, doi:10.1073/pnas.1604536113, 2016.

You, Y., Renbaum-Wolff, L., and Bertram, A. K.: Liquid-liquid phase separation in particles containing organics mixed with ammonium sulfate, ammonium bisulfate, ammonium nitrate or sodium chloride, Atmos. Chem. Phys., 13, 11723–11734, doi:10.5194/acp-13-11723-2013, 2013.

You, Y., Smith, M. L., Song, M., Martin, S. T., and Bertram, A. K.: Liquid–liquid phase separation in atmospherically relevant particles consisting of organic species and inorganic salts, Int. Rev. Phys. Chem., 33, 43–77, doi:10.1080/0144235x.2014.890786, 2014.

You, Y. and Bertram, A. K.: Effects of molecular weight and temperature on liquid-liquid phase separation in particles containing organic species and inorganic salts, Atmos. Chem. Phys., 15, 1351–1365, doi:10.5194/acp-15-1351-2015, 2015.

Zhang, Q., Jimenez, J. L., Canagaratna, M. R., Allan, J. D., Coe, H., Ulbrich, I., Alfarra, M. R., Takami, A., Middlebrook, A. M., Sun, Y. L., Dzepina, K., Dunlea, E., Docherty, K., DeCarlo, P. F., Salcedo, D., Onasch, T., Jayne, J. T., Miyoshi, T., Shimono, A., Hatakeyama, S., Takegawa, N., Kondo, Y., Schneider, J., Drewnick, F., Borrmann, S., Weimer, S., Demerjian, K., Williams, P., Bower, K., Bahreini, R., Cottrell, L., Griffin, R. J., Rautiainen, J., Sun, J. Y., Zhang, Y. M., and Worsnop, D. R.: Ubiquity and dominance of oxygenated species in organic aerosols in anthropogenically-influenced Northern Hemisphere midlatitudes, Geophys. Res. Lett., 34, L13801, doi:10.1029/2007gl029979, 2007.

Supplement of Atmos. Chem. Phys., 17, 5703–5719, 2017
https://doi.org/10.5194/acp-17-5703-2017-supplement

Atmospheric Chemistry and Physics
Open Access
EGU

Supplement of

Fine particle pH and gas–particle phase partitioning of inorganic species in Pasadena, California, during the 2010 CalNex campaign

Hongyu Guo et al.

Correspondence to: Rodney J. Weber (rweber@eas.gatech.edu) and Athanasios Nenes (athanasios.nenes@gatech.edu)

1. Comparisons of inorganic species measurements between AMS (PM_1) and PILS-IC ($PM_{2.5}$)

Consistency ($R^2 \geq 0.8$) between AMS and PILS-IC was observed. AMS measured nominally PM_1, whereas PILS-IC measured $PM_{2.5}$. These results are similar with other inter-comparisons reported elsewhere (Hayes et al., 2013). A larger difference in slope for nitrate than sulfate is thought to be due to higher nitrate concentrations in the 1 to 2.5 µm size range. $PM_1/PM_{2.5}$ mass ratios, reported in the main text, differ from slopes shown below due to differences in contributions of lower concentrations to these parameters (ratio vs. slope).

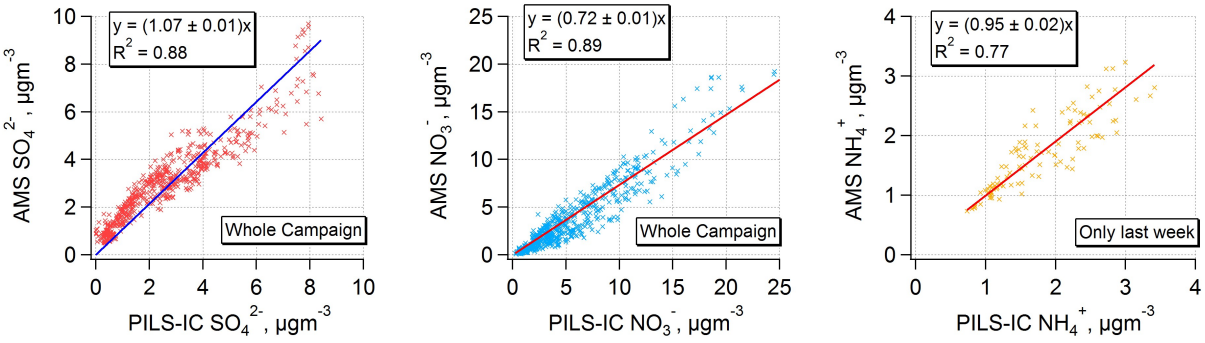

Fig. S1. Comparisons of PM_1 AMS sulfate, nitrate, ammonium to $PM_{2.5}$ PILS-IC (complete CalNex study except ammonium only for last week). Orthogonal distance regression (ODR) fits with fixed zero intercepts were applied. Fit slope uncertainty is one standard deviation.

2. The dependencies of nitrate, ammonium, and chloride on pH, W_i, and T (S curve equation derivations)

2.1 HNO_3-NO_3^- partitioning

The S curve of $\varepsilon(NO_3^-)$ has been discussed explicitly and compared to observations from WINTER aircraft campaign in Guo et al. (2016). Here we show the detailed derivation of equation (3) in that paper. Equilibrium between gaseous HNO_3 and particle-phase NO_3^- involves two processes, first dissolution of HNO_3 into aqueous phase (assuming particles are liquids) and second dissociation of dissolved HNO_3 into H^+ and NO_3^-. The two processes are reversible and often reach thermodynamic equilibriums at ambient conditions (RH, T) for fine particles.

$$1^{st} \quad HNO_{3(g)} \leftrightarrow HNO_3, \quad H_{HNO_3}$$

$$2^{nd} \quad HNO_3 \leftrightarrow NO_3^- + H^+, \quad K_{n1}$$

for which reaction equilibriums are expressed as follows,

$$H_{HNO_3} = \gamma_{HNO_3}[HNO_3]/p_{HNO_3} \tag{1}$$

$$K_{n1} = \frac{\gamma_{NO_3^-}[NO_3^-]\gamma_{H^+}[H^+]}{\gamma_{HNO_3}[HNO_3]} \tag{2}$$

where H_{HNO_3} is HNO_3 Henry's law constant, K_{n1} is HNO_3 acid dissociation constant, γ represents activity coefficient, p_{HNO_3} is partial pressure of HNO_3 in atmosphere, and [x] represents aqueous concentrations (mole L^{-1}). From equations (1) and (2) we get the total dissolved HNO_3 or total particle-phase nitrate (NO_3^T) as

$$[NO_3^T] = [HNO_3] + [NO_3^-] = H_{HNO_3}p_{HNO_3}\left(\frac{1}{\gamma_{HNO_3}} + \frac{K_{n1}}{\gamma_{NO_3^-}\gamma_{H^+}[H^+]}\right) \tag{3}$$

Ideal gas law gives

$$c(HNO_3) = \frac{p_{HNO_3}}{RT} \tag{4}$$

where c(x) represents concentration per volume of air (mole m^{-3}). Therefore, the particle-phase fraction of nitrate is

$$\varepsilon(NO_3^T) = \frac{c(NO_3^T)}{c(HNO_3) + c(NO_3^T)} = \frac{[NO_3^T]W_i}{c(HNO_3) + [NO_3^T]W_i} \tag{5}$$

where W_i is the particle liquid water content associated with inorganic species (μg m^{-3}; mass per volume of air) (here the organics associated liquid water is not considered, but it can be included, or measured particle water can be used). Taking equations (3) and (4) into (5), we get $\varepsilon(NO_3^T)$ as

$$\varepsilon(NO_3{}^{\mathrm{T}}) = \frac{\left(\frac{\gamma_{NO_3}{}^{-}\gamma_{H^+}}{\gamma_{HNO_3}}[H^+] + K_{n1}\right) H_{HNO_3} W_i RT}{\gamma_{NO_3}{}^{-}\gamma_{H^+}[H^+] + \left(\frac{\gamma_{NO_3}{}^{-}\gamma_{H^+}}{\gamma_{HNO_3}}[H^+] + K_{n1}\right) H_{HNO_3} W_i RT} \quad (6)$$

At 298 K, K_{n1}=12 mole L^{-1} (Fountoukis and Nenes, 2007) often >> $\frac{\gamma_{NO_3}{}^{-}\gamma_{H^+}}{\gamma_{HNO_3}}[H^+]$, so we assume $\left(\frac{\gamma_{NO_3}{}^{-}\gamma_{H^+}}{\gamma_{HNO_3}}[H^+] + K_{n1}\right) \approx K_{n1}$. Thus, a simplified equation is

$$\varepsilon\left(NO_3{}^{\mathrm{T}}\right) \cong \frac{K_{n1} H_{HNO_3} W_i RT}{\gamma_{NO_3}{}^{-}\gamma_{H^+}[H^+] + K_{n1} H_{HNO_3} W_i RT} \quad (7)$$

$H_{HNO_3} K_{n1}$ is denoted as $H^*_{HNO_3}$ (mole^2 kg^{-2} atm^{-1}) hereafter, which is equilibrium constant of the combined dissolution and deprotonation processes as,

$$HNO_{3(g)} \leftrightarrow NO_3{}^{-} + H^+, \;\; H^*_{HNO_3}$$

$H^*_{HNO_3}$ can be easily calculated by equation (40) in Clegg and Brimblecombe (1990) for T dependence and converted from unit atm^{-1} (mole fraction based) to mole^2 kg^{-2} atm^{-1} (molality based) by equation (5) also in that paper. To be consistent with SI units, we have the following equation ready for users' input:

$$\begin{aligned} \varepsilon\left(NO_3{}^{\mathrm{T}}\right) &\cong \frac{H^*_{HNO_3} W_i RT \times 0.987 \times 10^{-14}}{\gamma_{NO_3}{}^{-}\gamma_{H^+}[H^+] + H^*_{HNO_3} W_i RT \times 0.987 \times 10^{-14}} \\ &= \frac{H^*_{HNO_3} W_i RT \times 0.987 \times 10^{-14}}{\gamma_{NO_3}{}^{-}\gamma_{H^+} 10^{-pH} + H^*_{HNO_3} W_i RT \times 0.987 \times 10^{-14}} \end{aligned} \quad (8)$$

Note that 0.987 comes from the conversion from 1 atm to 1 bar and W_i unit is μg m^{-3}. Equation (8) describes the dependence of HNO_3-NO_3^- partitioning on pH, T, and W_i (determined by RH and aerosol composition). Based on ideal and non-ideal aqueous particles, several $\varepsilon(NO_3{}^{-})$ S curves at atmosphere relevant conditions are plotted together with $\varepsilon(Cl^-)$ and $\varepsilon(NH_4{}^{+})$ in Fig S3 and S4, respectively.

$\varepsilon\left(NO_3{}^{\mathrm{T}}\right)$ is equivalent to $\varepsilon(NO_3{}^{-})$ in the main text, since NO_3^- is practically 100% of $NO_3{}^{\mathrm{T}}$ based on $K_{n1} \gg \frac{\gamma_{NO_3}{}^{-}\gamma_{H^+}}{\gamma_{HNO_3}}[H^+]$ (also under atmospheric condition). The fraction of NO_3^- over $NO_3{}^{\mathrm{T}}$ can be given as

$$\frac{[NO_3{}^{-}]}{[NO_3{}^{\mathrm{T}}]} = \frac{K_{n1}}{K_{n1} + \frac{\gamma_{NO_3}{}^{-}\gamma_{H^+}}{\gamma_{HNO_3}}[H^+]} \quad (9)$$

2.2 HCl-Cl$^-$ partitioning

Following the same derivation procedure as HNO_3-NO_3^- partitioning, we have ε(Cl^-) as

$$\varepsilon(Cl^-) \cong \frac{H^*_{HCl} W_i RT \times 0.987 \times 10^{-14}}{\gamma_{Cl^-}\gamma_{H^+}[H^+] + H^*_{HCl} W_i RT \times 0.987 \times 10^{-14}} = \frac{H^*_{HCl} W_i RT \times 0.987 \times 10^{-14}}{\gamma_{Cl^-}\gamma_{H^+}10^{-pH} + H^*_{HCl} W_i RT \times 0.987 \times 10^{-14}} \quad (10)$$

where H^*_{HCl} (mole^2 kg^{-2} atm^{-1}) is the equilibrium constant and is equal to the "conventional" Henry's law constant multiplied by the acid dissociation constant of hydrochloric acid. H^*_{HCl} can be calculated by equation (22) in Carslaw et al. (1995) to account for T's variation.

$$HCl_{(g)} \leftrightarrow Cl^- + H^+, \quad H^*_{HCl}$$

A comparison of $\varepsilon(Cl^-)$ S curve with a subset of CalNex data is shown in Fig. S2. The selected CalNex data are all in a small range of T 15.5 to 19.5 ºC (around campaign average T) and W_i 10 to 20 µg m^{-3}, while the S curve is calculated based on the average condition of these data as T = 17.5 ºC, W_i = 15 µg m^{-3}, $\gamma_{H^+-Cl^-}$ = 0.81 (The binary activity coefficient, $\gamma_{H^+-Cl^-} = \sqrt{\gamma_{H^+}\gamma_{Cl^-}}$). The distribution of the $\varepsilon(Cl^-)$ points close to S curve validates the $PM_{2.5}$ pH prediction and demonstrates the usage of S curve.

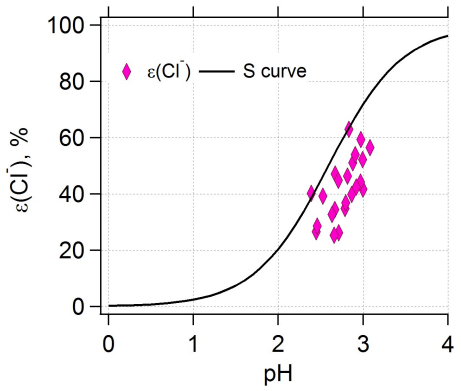

Fig. S2. The comparison of S curve and measured ε(Cl$^-$) with predicted particle pH by ISORROPIA-II. Cl$^-$ is from $PM_{2.5}$ PILS-IC measurements.

2.3 NH_3-NH_4^+ partitioning

The derivation of NH_3-NH_4^+ partitioning is a bit different from the above two acidic gases. Equilibrium between gaseous NH_3 and NH_4^+ can be described simply as

$$NH_{3(g)} + H^+ \leftrightarrow NH_4^+, \quad H^*_{NH_3}$$

($H^*_{NH_3}$ is equivalent to the "conventional" Henry's law constant of NH_3 divided by the acid dissociation constant of NH_4^+) or described by the follow two reversible reactions assuming water activity as unity.

$$1^{st}\ \ NH_{3(g)} \leftrightarrow NH_3, \qquad H_{NH_3}$$
$$2^{nd}\ \ NH_3 + H^+ \leftrightarrow {NH_4}^+, \ \ 1/K_a$$

for which reaction equilibriums are described as

$$H_{NH_3} = \gamma_{NH_3}[NH_3]/p_{NH_3} \tag{11}$$

$$1/K_a = \frac{\gamma_{{NH_4}^+}[{NH_4}^+]}{\gamma_{NH_3}[NH_3]\gamma_{H^+}[H^+]} \tag{12}$$

where H_{NH_3} is NH_3 Henry's law constant, K_a is NH_4^+ acid dissociation constant, γ represents activity coefficient, p_{NH_3} is partial pressure of NH_3 in atmosphere, and [x] represents aqueous concentrations (mole L^{-1}). Please note that the 2nd reaction is usually written in another form (Fountoukis and Nenes, 2007) as

$$2^{nd}\ \ NH_3 + H_2O \leftrightarrow {NH_4}^+ + OH^-, \ \ K_w/K_a$$

where K_w is water dissociation constant. Equations (10) and (11) give the total dissolved NH_3 or total particle-phase ammonium (${NH_4}^T$) as

$$[NH_4^T] = [NH_3] + [{NH_4}^+] = H_{NH_3}p_{NH_3}\left(\frac{1}{\gamma_{NH_3}} + \frac{\gamma_{H^+}[H^+]}{\gamma_{{NH_4}^+}K_a}\right) \tag{13}$$

Combining with ideal gas law, that is

$$c(NH_3) = \frac{p_{NH_3}}{RT} \tag{14}$$

where c(x) represents concentration per volume of air (mole m^{-3}). We have the particle-phase fraction of ammonium as

$$\varepsilon({NH_4}^T) = \frac{c(NH_4^T)}{c(NH_3) + c(NH_4^T)} = \frac{[NH_4^T]W_i}{c(NH_3) + [NH_4^T]W_i} \tag{15}$$

With equations (12) and (13), the above equation is transformed into

$$\varepsilon({NH_4}^T) = \frac{\left(\frac{\gamma_{H^+}[H^+]}{\gamma_{{NH_4}^+}} + \frac{K_a}{\gamma_{NH_3}}\right)\frac{H_{NH_3}}{K_a}W_iRT}{1 + \left(\frac{\gamma_{H^+}[H^+]}{\gamma_{{NH_4}^+}} + \frac{K_a}{\gamma_{NH_3}}\right)\frac{H_{NH_3}}{K_a}W_iRT} \tag{16}$$

At 298 K, K_a = 5.69×10^{-10} mole L^{-1} (Clegg et al., 1998) results in $\frac{K_a}{\gamma_{NH_3}} \ll \frac{\gamma_{H^+}[H^+]}{\gamma_{{NH_4}^+}}$ as long as the solution is not too basic. Neglecting $\frac{K_a}{\gamma_{NH_3}}$ part and taking $\frac{H_{NH_3}}{K_a} = H^*_{NH_3}$, we have

$$\varepsilon({NH_4}^T) \cong \frac{\frac{\gamma_{H^+}[H^+]}{\gamma_{{NH_4}^+}}H^*_{NH_3}W_iRT}{1 + \frac{\gamma_{H^+}[H^+]}{\gamma_{{NH_4}^+}}H^*_{NH_3}W_iRT} \tag{17}$$

To be consistent with SI units, the equation (16) is then presented as:

$$\varepsilon\left(NH_4{}^{\mathrm{T}}\right) \cong \frac{\frac{\gamma_{H^+}[H^+]}{\gamma_{NH_4{}^+}} H^*_{NH_3} W_i RT \times 0.987 \times 10^{-14}}{1 + \frac{\gamma_{H^+}[H^+]}{\gamma_{NH_4{}^+}} H^*_{NH_3} W_i RT \times 0.987 \times 10^{-14}} = \frac{\frac{\gamma_{H^+} 10^{-pH}}{\gamma_{NH_4{}^+}} H^*_{NH_3} W_i RT \times 0.987 \times 10^{-14}}{1 + \frac{\gamma_{H^+} 10^{-pH}}{\gamma_{NH_4{}^+}} H^*_{NH_3} W_i RT \times 0.987 \times 10^{-14}} \quad (18)$$

where the 0.987 comes from the conversion from 1 atm to 1 bar and W_i unit is μg m^{-3}. $H^*_{NH_3}$(atm^{-1}) can be calculated from equation (12) in Clegg et al. (1998) following a typo correction to the equation. The corrected equation is:

$$\ln\left(H^*_{NH_3}\right) = 25.393 - 10373.6(1/T_r - 1/T) + 4.131\left(T_r/T - (1 + \ln(T_r/T))\right) \quad (19)$$

where T_r is the reference temperature of 298.15 K. Note that, the mole fraction based $H^*_{NH_3}$ has the same numerical value as its molality based form. After correction, a larger $H^*_{NH_3}$ is associated with a lower temperature, consistent with a general expectation that NH_3 condenses onto particles if temperature decreases. $\varepsilon(NH_4{}^{\mathrm{T}})$ is equivalent to $\varepsilon(NH_4^+)$ presented in the main text, since NH_4^+ is the dominant form of dissolved NH_3 based on $\frac{K_a}{\gamma_{NH_3}} \ll \frac{\gamma_{H^+}[H^+]}{\gamma_{NH_4{}^+}}$ and under atmospheric conditions.

Summary: with the equations of $\varepsilon(NO_3^-)$, $\varepsilon(Cl^-)$, and $\varepsilon(NH_4^+)$, S-shaped curves of these three paired gas to particle partitioning can be easily calculated with pH, T, W_i, and activity coefficients. We simulate two set of results, Fig S3 assuming activity coefficients to be one (ideal solution) and Fig S4 with practical activity coefficients from CalNex.

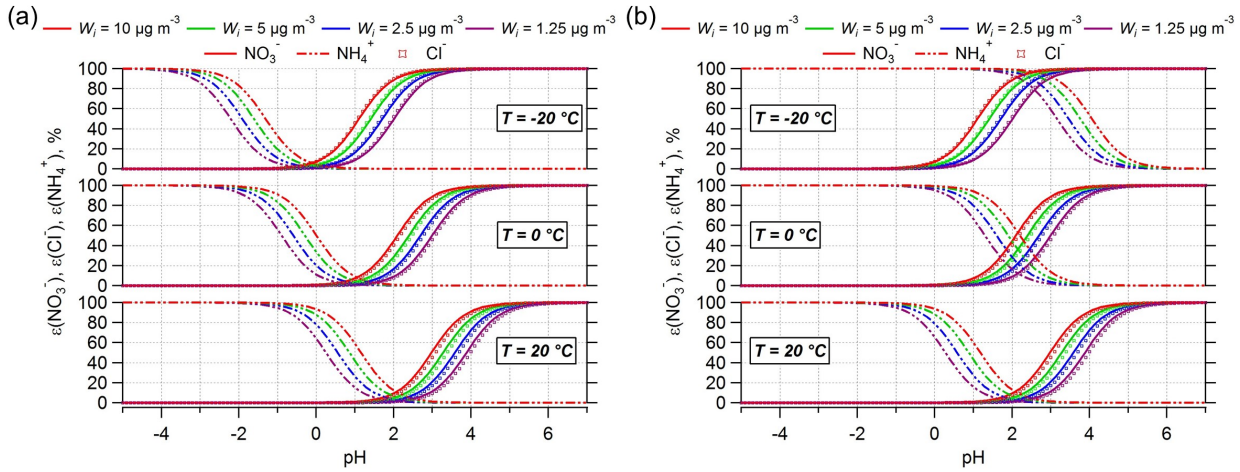

Fig. S3. Simulated ε(NO_3^-), ε(NH_4^+), ε(Cl^-) at -20 °C, 0 °C, 20 °C and various particle liquid water levels (1.25, 2.5, 5, 10 µg m^{-3}) assuming ideal solutions. Note that Fig. S3a shows ε(NH_4^+) calculated using the equation (12) in Clegg et al. (1998), and Fig. S3b shows ε(NH_4^+) using the corrected equation, given above as equation (19). The correct equation for $H^*_{NH_3}$ shifts ε(NH_4^+) to higher pH at lower T, as expected.

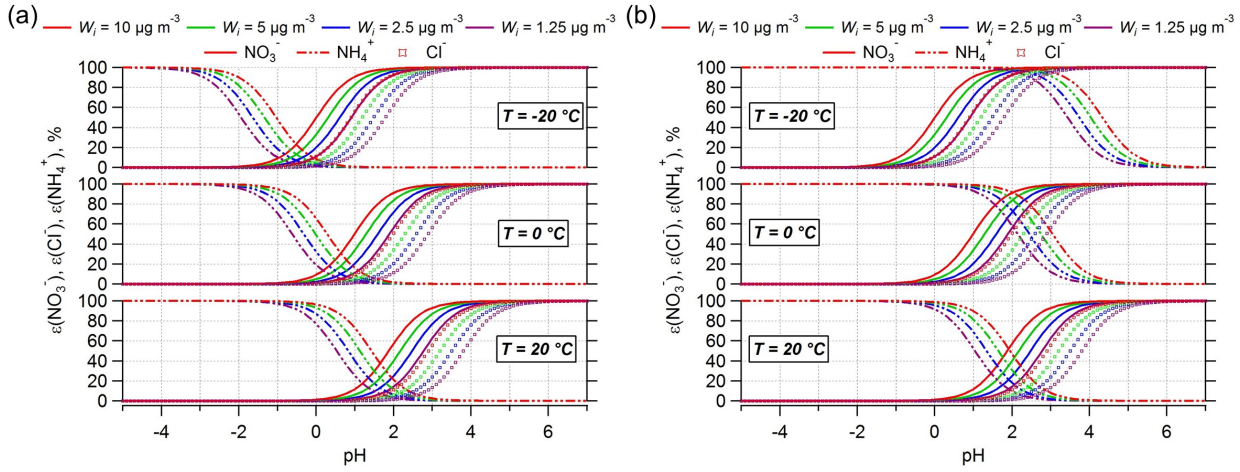

Fig. S4. Simulated ε(NO_3^-), ε(NH_4^+), ε(Cl^-) at -20 °C, 0 °C, 20 °C and various particle liquid water levels (1.25, 2.5, 5, 10 µg m^{-3}) with activity coefficients obtained from CalNex campaign. $\gamma_{H^+-NO_3^-}$ = 0.28, $\gamma_{H^+-Cl^-}$ = 0.81, and $\gamma_{H^+}/\gamma_{NH_4^+}$ = 1.90. Similar to Fig. S3, Fig. S4a shows ε(NH_4^+) calculated using the equation (12) in Clegg et al. (1998), and Fig. S4b shows ε(NH_4^+) using the corrected equation, given above as equation (19).

3. Investigation of the cause for bias in ε(NO_3^-): sample line heating?

As Fig. S5 shows, NO_3^- and ε(NO_3^-) are both over-predicted during the nighttime and under-predicted during the daytime. The deviations from measurements are anti-correlated with nitric acid. The deviation between predicted and measured HNO_3 also has a diurnal pattern, reverse to that of NO_3^-.

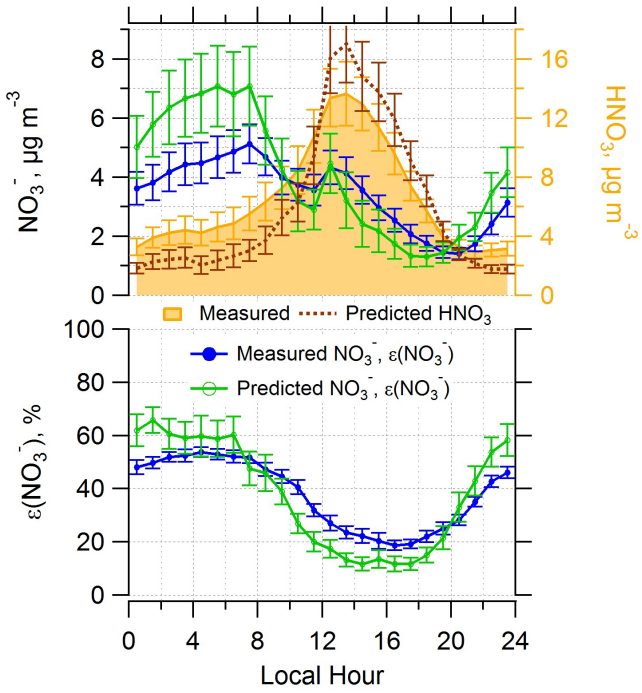

Fig. S5. Diurnal profiles of measured and predicted HNO_3, NO_3^-, and ε(NO_3^-). Data shown above are for the complete CalNex study and particle-phase data is AMS PM_1. Mean hourly averages are shown and standard errors are plotted as error bars.

Table S1. Summary of temperature differences in sample lines and ambient and sample line residence time for the AMS and CIMS. AMS indoor T was 25°C. CIMS inlet was heated to 75°C.

Instrument	Inlet residence time, sec	Time of the day	Temperature differences, °C
AMS	2.1	Day	~0
		Night	~ +10
CIMS	0.32	Day	~ +50
		Night	~ +60

For the AMS sample line located indoors, particle heating was most likely to occur at night (indoor T > ambient T), which may cause semi-volatile NO_3^- loss. There were no temperature differences during the day (Table S1). To examine the possible sample line heating/cooling effect, we first determined sample line RH (Equation 20) by conservation of water vapor under isobaric condition and following saturated water vapor pressure equation $e_s = 6.11\times10^{\left(\frac{7.5T}{237.5+T}\right)}$ (T unit as °C) (Alduchov and Eskridge, 1996). The inferred sample line RH is plotted with measured ambient RH in Fig. S6b. Sample line RH was lower (~50%) than ambient (~90%) at midnight and close to ambient (~60%) in the afternoon since temperatures were similar.

$$RH_2 = RH_1 10^{\left[\left(\frac{7.5T_1}{237.5+T_1}\right)-\left(\frac{7.5T_2}{237.5+T_2}\right)\right]} \quad (20)$$

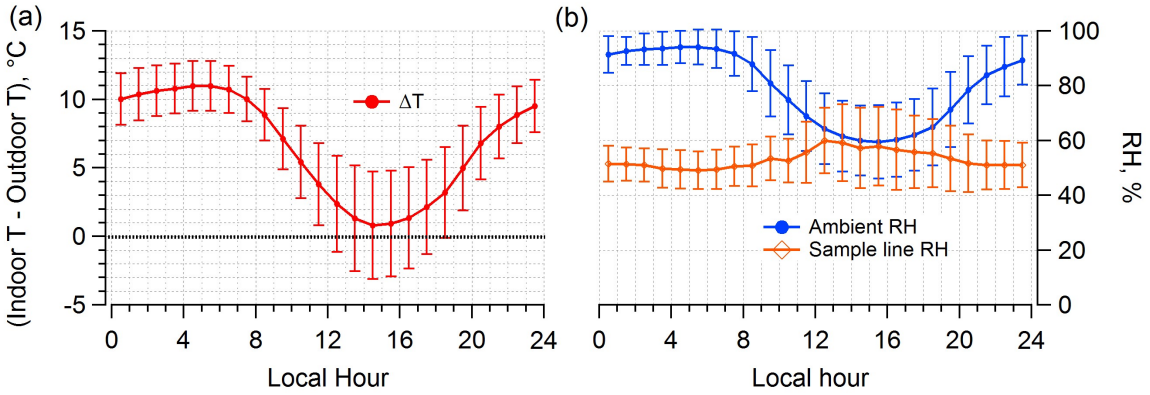

Fig. S6. Diurnal profiles of (a) temperature difference between AMS indoor and outdoor and (b) corresponding ambient and RH predicted in the sample line due to the T difference. Mean hourly averages and standard deviations are shown.

ISORROPIA-II was run with aerosol and gas-phase species at the AMS sample line T and RH and compared to predictions from ambient T and RH and measurements. Fig. S7 is discussed in the main text section 4.1.

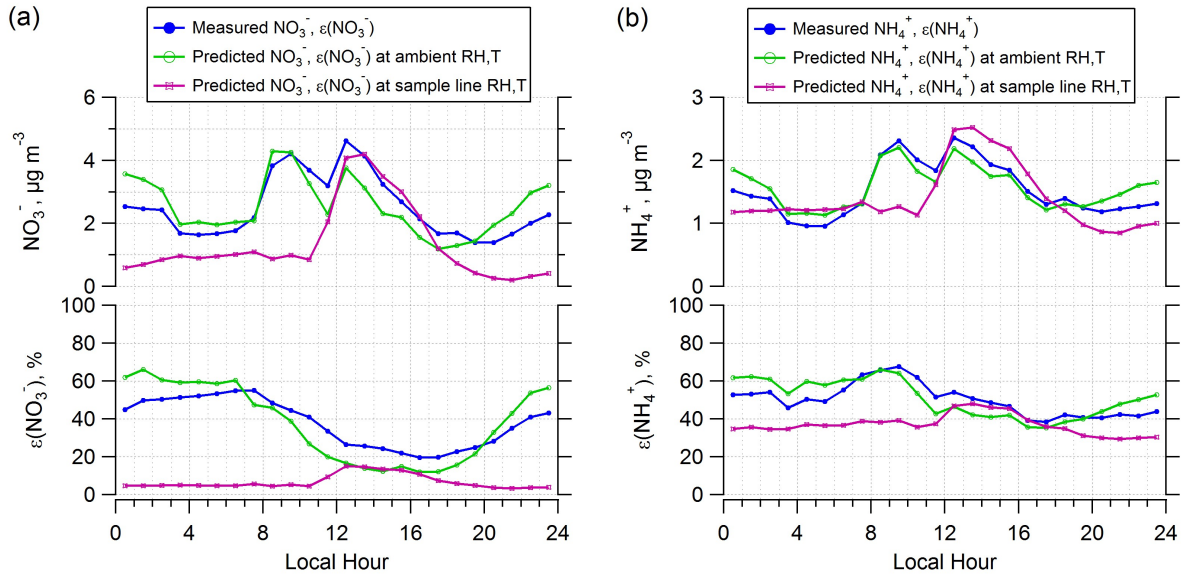

Fig. S7. Diurnal profiles of measured and predicted (a) NO_3^-, $\varepsilon(NO_3^-)$ and (b) NH_4^+, $\varepsilon(NH_4^+)$. Predictions are based on ambient or sample line RH and T for AMS inlet. Data shown above are for the complete CalNex study in the 20-95% RH range and particle-phase data is AMS PM_1. Mean hourly averages are shown. ISORROPIA run with ambient data show that the predicted partitioning between the particle and gas phase is in better agreement with observations than runs using sample line T and RH. Note that in both runs, only T and RH differ since total nitrate and ammonium input are the same.

CIMS inlet heating is similar for day (~50°C) and night (~60°C). Potential bias in the HNO_3 or HCl then mainly depends on the mass loadings of NO_3^- or Cl^-. Here we focus only on the possible bias due to over-measurement of HNO_3. ISORROPIA-II was run at ambient RH and T with a "corrected" HNO_3 at three assumed lower levels of HNO_3 to compensate for an assumed positive nitrate artifact of 10%, 20%, 30% (i.e., assuming 10, 20 or 30% of the nitrate measured by the AMS or PILS was evaporated in the CIMS inlet leading to an over-measurement of HNO_3. 10% to 30% particle NO_3^- was subtracted from the measured CIMS HNO_3). Only HNO_3 is modified, all other inputs are kept the same. Results are shown in Fig. S8. Evaporation of 30% of the measured nitrate is expected to be an extreme upper limit. For instance, 66% of PM_1 nitrate evaporated at a temperature of 75°C in a thermal denuder upstream of the AMS at the CalNex site, consistent with previous results at other urban sites in the LA area and elsewhere (Huffman et al., 2009). The residence time on the thermal denuder was ~ 12 sec, while that of the CIMS inlet was ~0.32 sec, so the extent of evaporation in the CIMS inlet assumed to be substantially lower than that in the thermal denuder.

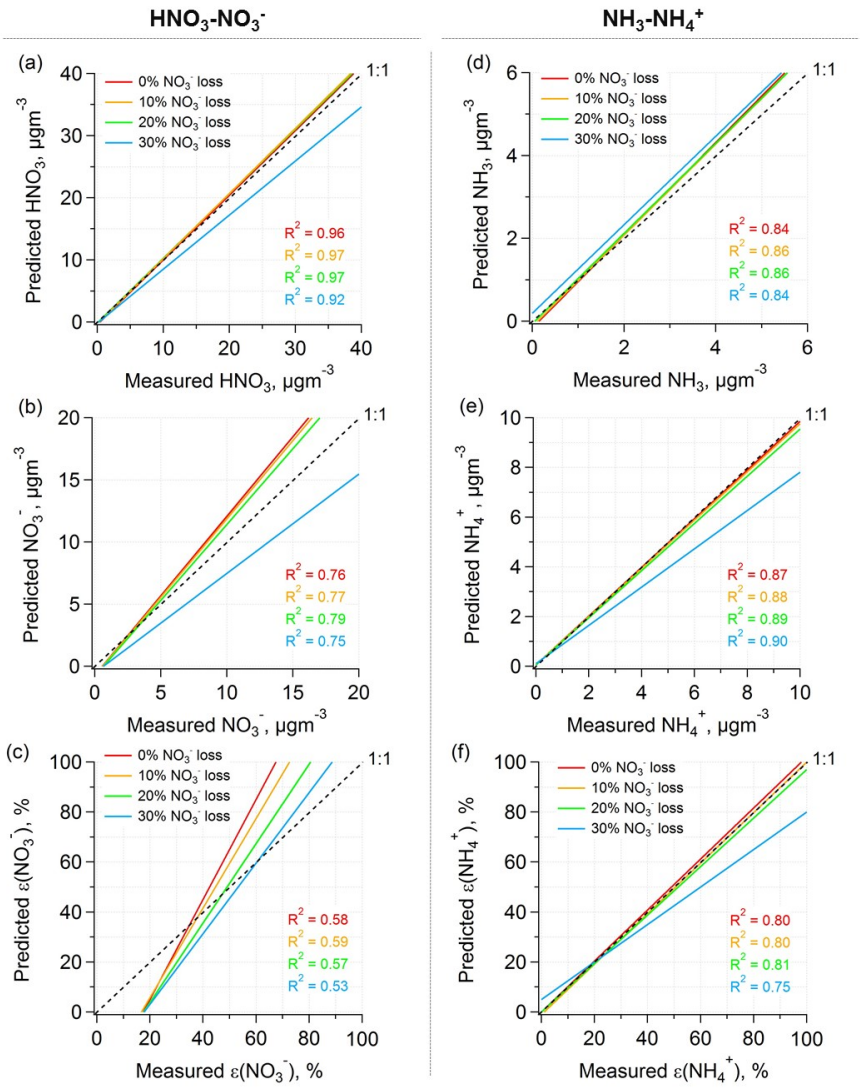

Fig. S8. Comparisons of predicted and measured HNO_3, NO_3^-, and $\varepsilon(NO_3^-)$ (a, b, c) and NH_3, NH_4^+, and $\varepsilon(NH_4^+)$ (d, e, f) for data from the complete CalNex study based on "corrected" HNO_3 data due to assumed PM_1 nitrate evaporation in the heated CIMS inlet. The other inputs are kept the same. Only the orthogonal regression fits are shown. "0% NO_3^- loss" condition is the same as Figure 2 in the main text.

References

Alduchov, O. A., and Eskridge, R. E.: Improved magnus form approximation of saturation vapor pressure, J Appl Meteorol, 35, 601-609, doi: 10.1175/1520-0450(1996)035<0601:Imfaos>2.0.Co;2, 1996.

Carslaw, K. S., Clegg, S. L., and Brimblecombe, P.: A Thermodynamic Model of the System HCl-HNO_3-H_2SO_4-H_2O, Including Solubilities of Hbr, from <200 to 328 K, Journal of Physical Chemistry, 99, 11557-11574, doi: 10.1021/j100029a039, 1995.

Clegg, S. L., and Brimblecombe, P.: Equilibrium Partial Pressures and Mean Activity and Osmotic Coefficients of 0-100-Percent Nitric-Acid as a Function of Temperature, Journal of Physical Chemistry, 94, 5369-5380, doi: 10.1021/j100376a038, 1990.

Clegg, S. L., Brimblecombe, P., and Wexler, A. S.: Thermodynamic model of the system H^+-NH_4^+-SO_4^{2-}-NO_3^--H_2O at tropospheric temperatures, J Phys Chem A, 102, 2137-2154, doi: 10.1021/Jp973042r, 1998.

Fountoukis, C., and Nenes, A.: ISORROPIA II: a computationally efficient thermodynamic equilibrium model for K^+-Ca^{2+}-Mg^{2+}-NH_4^+-Na^+-SO_4^{2-}-NO_3^--Cl^--H_2O aerosols, Atmospheric Chemistry and Physics, 7, 4639-4659, doi: 10.5194/acp-7-4639-2007, 2007.

Guo, H., Sullivan, A. P., Campuzano-Jost, P., Schroder, J. C., Lopez-Hilfiker, F. D., Dibb, J. E., Jimenez, J. L., Thornton, J. A., Brown, S. S., Nenes, A., and Weber, R. J.: Fine particle pH and the partitioning of nitric acid during winter in the northeastern United States, Journal of Geophysical Research: Atmospheres, 121, 10,355-310,376, doi: 10.1002/2016jd025311, 2016.

Hayes, P. L., Ortega, A. M., Cubison, M. J., Froyd, K. D., Zhao, Y., Cliff, S. S., Hu, W. W., Toohey, D. W., Flynn, J. H., Lefer, B. L., Grossberg, N., Alvarez, S., Rappenglück, B., Taylor, J. W., Allan, J. D., Holloway, J. S., Gilman, J. B., Kuster, W. C., de Gouw, J. A., Massoli, P., Zhang, X., Liu, J., Weber, R. J., Corrigan, A. L., Russell, L. M., Isaacman, G., Worton, D. R., Kreisberg, N. M., Goldstein, A. H., Thalman, R., Waxman, E. M., Volkamer, R., Lin, Y. H., Surratt, J. D., Kleindienst, T. E., Offenberg, J. H., Dusanter, S., Griffith, S., Stevens, P. S., Brioude, J., Angevine, W. M., and Jimenez, J. L.: Organic aerosol composition and sources in Pasadena, California, during the 2010 CalNex campaign, Journal of Geophysical Research: Atmospheres, 118, 9233-9257, doi: 10.1002/jgrd.50530, 2013.

Huffman, J. A., Docherty, K. S., Aiken, A. C., Cubison, M. J., Ulbrich, I. M., DeCarlo, P. F., Sueper, D., Jayne, J. T., Worsnop, D. R., Ziemann, P. J., and Jimenez, J. L.: Chemically-resolved aerosol volatility measurements from two megacity field studies, Atmospheric Chemistry and Physics, 9, 7161-7182, doi: 10.5194/acp-9-7161-2009, 2009.